

SANDIA REPORT

SAND2012-8009

Unlimited Release

Printed September 2012

Stability of Fusion Target Concepts on Z

Daniel B. Sinars, Ryan McBride, Dean Rovang, Adam Sefkow, Stephen Slutz, Ray Lemke, Michael Cuneo, Mark Herrmann, Chris Jennings, Marc Jobe, Derek Lamppa, Matt Martin, Charlie Nakhleh, Albert Owen, John McKenney, Ray Mock, Todd Peters, Gerald Torres, Eduardo Waisman

Prepared by
Sandia National Laboratories
Albuquerque, New Mexico 87185 and Livermore, California 94550

Sandia National Laboratories is a multi-program laboratory managed and operated by Sandia Corporation, a wholly owned subsidiary of Lockheed Martin Corporation, for the U.S. Department of Energy's National Nuclear Security Administration under contract DE-AC04-94AL85000.

Approved for public release; further dissemination unlimited.



Issued by Sandia National Laboratories, operated for the United States Department of Energy by Sandia Corporation.

NOTICE: This report was prepared as an account of work sponsored by an agency of the United States Government. Neither the United States Government, nor any agency thereof, nor any of their employees, nor any of their contractors, subcontractors, or their employees, make any warranty, express or implied, or assume any legal liability or responsibility for the accuracy, completeness, or usefulness of any information, apparatus, product, or process disclosed, or represent that its use would not infringe privately owned rights. Reference herein to any specific commercial product, process, or service by trade name, trademark, manufacturer, or otherwise, does not necessarily constitute or imply its endorsement, recommendation, or favoring by the United States Government, any agency thereof, or any of their contractors or subcontractors. The views and opinions expressed herein do not necessarily state or reflect those of the United States Government, any agency thereof, or any of their contractors.

Printed in the United States of America. This report has been reproduced directly from the best available copy.

Available to DOE and DOE contractors from

U.S. Department of Energy
Office of Scientific and Technical Information
P.O. Box 62
Oak Ridge, TN 37831

Telephone: (865) 576-8401
Facsimile: (865) 576-5728
E-Mail: reports@adonis.osti.gov
Online ordering: <http://www.osti.gov/bridge>

Available to the public from

U.S. Department of Commerce
National Technical Information Service
5285 Port Royal Rd.
Springfield, VA 22161

Telephone: (800) 553-6847
Facsimile: (703) 605-6900
E-Mail: orders@ntis.fedworld.gov
Online order: <http://www.ntis.gov/help/ordermethods.asp?loc=7-4-0#online>



Stability of Fusion Target Concepts on Z

Daniel B. Sinars¹, Ryan McBride¹, Dean Rovang², Adam Sefkow³, Stephen Slutz³, Ray Lemke⁴, Michael Cuneo², Mark Herrmann⁵, Chris Jennings³, Marc Jobe⁶, Derek Lamppa⁶, Matt Martin⁴, Charlie Nakhleh³, Albert Owen⁷, John McKenney², Ray Mock², Todd Peters⁶, Gerald Torres⁸, Eduardo Waisman²

- (1) High Energy Density Experiments, Org. 1648
- (2) Radiation and Fusion Experiments, Org. 1643
- (3) Inertial Confinement Fusion Target Design, Org. 1644
- (4) High Energy Density Physics Theory, Org. 1641
- (5) High Energy Density Science, Org. 1640
- (6) Electromagnetic Launch Systems, Org. 5445
- (7) Pulsed Power Engineering, Org. 1676
- (8) Above-ground-test Accelerator Operations, Org. 1342

Sandia National Laboratories
P.O. Box 5800
Albuquerque, New Mexico, 87185-MS1193

Abstract

The key scientific issue for magnetically driven fusion concepts is the stability of the cylindrical liner surrounding the fuel. The liner is susceptible to the magneto-Rayleigh-Taylor instability, which can disrupt the liner implosion and prevent it from successfully compressing and confining the fuel. We summarize an LDRD project to investigate the stability of aluminum and beryllium liner implosions on the Sandia Z pulsed power facility. Much of the work was conducted in the specific context of a new magnetized liner inertial fusion (MagLIF) concept, and continued modeling of that concept was supported by this project. However, the liner stability data is fundamental to magnetically driven systems, and the idea of magnetizing and preheating fuel applies to any inertial confinement fusion platform. We also demonstrated prototype 10 T axial magnetic field coils, which are needed both to test the MagLIF concept and the idea of stabilizing liner implosions using magnetic fields.

ACKNOWLEDGMENTS

We thank the many Z and Z-Beamlet operations and production teams for their excellent support of the liner stability experiments on Z that were undertaken as part of this project.

We thank General Atomics for their support in developing and fabricating the liner targets fielded on the Z facility. Much of the work described here would not have been possible without the development of a beryllium machining capability in La Jolla, CA.

We thank Ron Kaye (Manager, Org. 5445) for supporting the development of the Systems Integration and Test Facility in his laboratory space and for the use of Derek Lamppa and Marc Jobe to support the development of magnetic field coils.

We thank Jim Puissant (Org. 1647) for supporting the magnetic field coil design and testing activities.

We thank TJ Rogers (formerly Org. 1678) for designing the raised power-feed hardware for Z that is compatible with the magnetic field coils, and was tested during the “Washington” shots.

We thank Dawn Flicker (Manager, Org. 1646) for supporting the collaboration between the ICF and Dynamic Materials program that enabled the “Union” experiments on Z. These experiments, while explicitly aimed at studying the equation of state of beryllium using cylindrical liners, are also relevant to ICF implosions and the techniques may ultimately benefit MagLIF.

We thank the code support teams at LLNL for both LASNEX and HYDRA for helping us to advance the simulations conducted as part of this project. We also thank the support staff at numerous computing platforms at both SNL and LLNL who helped shepherd the simulations through to completion.

We thank Adam Harvey-Thompson (Org. 1643), Eric Harding (Org. 1648), Matthias Geissel (Org. 1672), and Ian Smith (Org. 1672) for useful discussions on using the Z-Beamlet laser for preheating, which was integrated into the HYDRA simulations presented here.

We thank Steve Nickerson (Org. 10616) in the 1600 Business Services office for helping us with cost estimates and planning related to this LDRD project.

CONTENTS

1. Introduction.....	11
2. Liner stability experiments on Z.....	15
2.1 Overview of Z experiments	15
2.2 Single-mode Magneto-Rayleigh-Taylor experiments.....	18
2.3 Beryllium liner experiments studying multi-mode MRT growth.....	20
2.4 Enhanced-contrast beryllium liner experiments using Al sleeves	22
2.5 Experiments studying role of surface roughness on MRT growth	24
2.6 On the possibility of current pulse shaping to improve stability	27
2.7 The use of pulse-shaped liners for dynamic materials experiments	33
3. Development of Magnetic Field System.....	35
3.1 Introduction.....	35
3.2 Capacitor bank system development	36
3.3 Road map for coil design and development.....	37
3.4 Demonstration of a 10 T, full diagnostic access MagLIF prototype	39
3.5 Z experiments studying power flow in coil-compatible hardware	42
3.6 Design status of experimental hardware for the first magnetized preheat and magnetized Z experiments in 2013	44
4. Modeling of magnetized liner fusion concept	47
4.1 Introduction.....	47
4.2 High-yield, high-gain magnetized liner targets	48
4.3 Integrated MagLIF calculations using HYDRA.....	50
5. Invited presentations, publications, and awards supported by this project.....	55
5.1 Invited presentations	55
5.2 Publications.....	56
5.3 Awards received.....	57
6. References.....	59
Distribution	62

FIGURES

- Figure 1: An approach to ICF using the magnetically driven compression of cylindrical metal liners containing magnetized and preheated fusion fuel to the conditions needed for fusion. First, the target containing cold DT gas is magnetized with an axial magnetic field using external field coils (not shown). A laser pulse subsequently heats the fuel to ~ 250 eV. A current driven through the cylinder produces an azimuthal magnetic field that implodes the shell, compressing the plasma to fusion conditions. 11
- Figure 2: Photographs of Al targets fabricated for use in the initial magneto-Rayleigh-Taylor experiments. The diameter of the targets shown is 0.25 inches (6.35 mm)..... 15
- Figure 3: Illustrations of the 2-frame 6.151 keV x-ray backlighting diagnostic for the Z facility. (a) Side-on half-section diagram of the 2-frame backlighter that illustrates the ± 3 -degree view

through the load above/below the horizontal. (b) Side-on-photograph of the diagnostic as installed on Z. (c) Top-down photograph of the diagnostic as installed on Z. 16

Figure 4: Hollow cylinders of aluminum (liners) were imploded on the Z machine during the first set of MRT experiments. Sinusoidal perturbations with wavelengths of 200 and 400 μm (and peak-to-valley amplitudes of 10 and 20 μm , respectively) were machined onto the outside surface of the liner, as shown in the photograph. This deformation was captured using x-ray radiography at 8 different times during the implosion as shown..... 18

Figure 5: Analysis of the 400- μm wavelength data from Figure 4. The peak-to-valley amplitude from experiments (black) is compared to simulations (Green) and analytic theory (blue). The decrease in amplitude between 18 and 40 ns is caused by plasma ablating from the liner surface. 19

Figure 6: (a) Radiographs of beryllium liner implosions. The latest (bottom) two frames captured the implosion just after the inner liner surface had stagnated on axis and while trailing liner material continued to flow into the stagnation column, compressing the column further. The vertical dashed lines indicate the initial positions of the inner and outer liner surfaces. (b-e) Synthetic radiographs from radiation-MHD simulations using the 3D GORGON code and the 2D LASNEX code. 20

Figure 7: Liner surface finish data. (a) Sample of surface height variation illustrating azimuthally-correlated structure (striations) due to the single-point, diamond-turned fabrication process (the liners were not polished or further modified). (b) Power spectra for axially-aligned wave vectors (600 μm axial sample length). The liner surface finishes had a root-mean-square roughness of 100-250 μm 21

Figure 8: Analysis of radiography data designed to enhance the contrast of the inner liner surface. The experiments shown used AR=6 beryllium liners with a 2- μm thick Al sleeve inserted just inside the inside surface of the beryllium. (a) The radiograph images in transmission units. (b) The same radiographs with the color range remapped to the 0-30% transmission to enhance the visibility of low-transmission features. (c) Density contour plots obtained from Abel transforms of the transmission data assuming cylindrical symmetry. These are only valid outside of the Al sleeve position. The interior structures seen in the top three radiographs are micro-B-dot probes used to measure the flux inside of the liner at early times. 23

Figure 9: Example surface characterization data collected with a Zygo interferometer. On the left side a 2D color contour plot of the depth of the surface is shown, with the axial direction of the cylinder along the vertical direction. On the right side a 3D rendering of the same data is shown. Unlike the data in Figure 7, there is no consistent azimuthal correlation of the surface structure. 24

Figure 10: Photo of an axially polished beryllium cylinder. 25

Figure 11: Radiographs from shots examining the impact of surface roughness on the growth and correlation of the MRT instability. 26

Figure 12: Timing of the radiographs with respect to the current pulse. The radiography data from Figure 6 were obtained at the times indicated by vertical blue lines. The radiography data from Figure 11 were obtained at the times indicated by vertical red and green lines. 26

Figure 13: Example radiograph from z2104 showing a sharp discontinuity in the density (opacity) of the liner due to a strong shock. The image on the left is shown from 0 to 100% transmission. In the left image the color scale was remapped to display the 0-30% transmission range in order to see the low-transmission regions more clearly..... 27

Figure 14: Axially averaged lineouts from radiographs of experiments (a) in which a strong shocked was launched, and (b) in which the current pulse was shaped specifically to avoid launching a shock in the liner. In both cases an AR=4 beryllium liner was used.	28
Figure 15: (a) Load current vs. time. (b) Simulated velocity of the liner inner surface vs. time..	29
Figure 16: Filled contours of simulated liner density for (a) z2104, and (b) z2207.	30
Figure 17: Simulated and measured density vs. position for z2107. Densities at time 3050.3 ns correspond to the radiograph in Figure 13.	30
Figure 18: Plot of the shear modulus G vs. time from ALEGRA simulations of z2104 and z2207, which illustrates that in the shockless case (z2207) the liner remains in the solid state with strength.	31
Figure 19: Plot of electrical conductivity vs. time from simulated shots z2104 and z2207.	31
Figure 20: Abel-inverted density profiles at six separate times as determined from experimental radiographs of beryllium liner implosions. Taken from [10].	33
Figure 21: Two capacitor bank modules stacked vertically.	36
Figure 22: Schematic of the capacitor bank integrated into the Z facility.	37
Figure 23: Standard low inductance power feed and load configuration. The example shown is from the "Lincoln 2" experiments in 2010.	38
Figure 24: Notional road map for MagLIF magnet system integration and development.	38
Figure 25: A 10-Tesla MagLIF prototype assembly with test windings of coils.	40
Figure 26: Cross-section of un-shot 80-turn top coil.	40
Figure 27: (a) A 10-T MagLIF prototype shown inside the SITF test chamber. (b) The measured field pulse recorded during an SITF experiment with this prototype.	41
Figure 28: Post-mortem cross-sections of prototype coil set #1 after a soft failure during its 18th pulse at 10 T. No obvious indicator of failure is visible.	41
Figure 29: Plot illustrating the dimensions of the three extended power feed geometries used in March 2012 "Washington-1" experiments on Z, compared with the standard power feed dimension used in most liner stability experiments.	43
Figure 30: (a) Plots of the upstream load B-dot current measured during Washington 1 experiments using an extended power feed, compared to a baseline experiment ("Lincoln") using a standard feed configuration. (b) Preliminary VISAR probe velocity unfolds for the Washington-1 experiments.	43
Figure 31: Conceptual design of MagLIF magnet system on a 31-cm convolute.	44
Figure 32: Schematic diagram of the design layout for all the diagnostics requested for magnetized preheating and Z experiments in 2013. The experiments will use the full-access configuration for the magnetic field coils.	44
Figure 33: Design layout showing final feed designs for the first magnetized experiments in 2013.	45
Figure 34: $J \times B$ force distribution on the upper anode from transient electromagnetic analysis ($t=1.25$ ms).	46
Figure 35: Calculated von Mises stresses from static mechanical finite element analysis of the upper anode. The stresses shown are from a 10-T magnetic field.	46
Figure 36: Schematic diagram of a high-gain, high-yield MagLIF target.	49
Figure 37: Simulated yields (solid curves) and gains (dashed curves) plotted as a function of peak drive current. The black curves are for standard MagLIF while the colored curves are the results for MagLIF simulations that include a cryogenic layer of DT ice on the inner surface of a liner (beryllium shown as red, aluminum as blue).	50

Figure 38: An example of the complex, multi-block mesh that is required in HYDRA in order to capture all of the relevant integrated details. This meshing allows for fine ablation zoning on all surfaces (where it is needed)..... 51

Figure 39: Example HYDRA simulation results from four selected times. The left plots indicate the density and the right plots the electron temperature, both on a log scale. The examples show the state (a) just prior to the start of current, (b) midway through the laser preheat pulse, (c) shortly after the preheated fuel has equilibrated, and (d) a few ns prior to stagnation..... 53

Figure 40: Example HYDRA plots indicating the final conditions achieved by a MagLIF target. The simulations shown are fully-integrated HYDRA calculations. 54

TABLES

Table 1: Summary of the 35 Z experiments to date relevant to liner stability studies. The campaign names relate to the primary goals of the experiments. The AR refers to the liner aspect ratio, defined as the outer liner diameter divided by its thickness. The MagLIF point designs assume a liner with AR=6, but a broad range of ARs may work. 17

Table 2: Key coil parameters for existing coil systems with coil lengths of 10 cm. 39

Table 3: Engineering safety factors for MagLIF targets..... 42

NOMENCLATURE

AR	aspect ratio, defined here as the initial liner outer radius divided by its thickness
B	magnetic field
Bz	magnetic field along the “z” direction (i.e., along axis of a cylinder)
CR	convergence ratio, defined as initial fuel radius divided by the final fuel radius
DD	deuterium (only) fusion fuel mixture
DOE	Department of Energy
DT	deuterium-tritium fusion fuel mixture (equimolar)
GORGON	An MHD code developed by Imperial College, London
HEDP	High Energy Density Physics (typically defined as having >1 Mbar pressure)
HYDRA	An inertial confinement fusion simulation code developed by LLNL
ICF	Inertial Confinement Fusion
LASNEX	An inertial confinement fusion simulation code developed by LLNL
LDRD	Laboratory Directed Research and Development
LEH	Laser Entrance Hole
LLNL	Lawrence Livermore National Laboratory
MA	Mega-Amperes (1,000,000 Amperes)
MagLIF	Magnetized Liner Inertial Fusion
MHD	magneto-hydrodynamics
MRT	magneto-Rayleigh-Taylor
SNL	Sandia National Laboratories
T	Tesla (unit of magnetic field strength)

1. INTRODUCTION

Pulsed-power-driven z-pinches have long been of interest as efficient plasma radiation sources with a demonstrated efficiency of ~15% (wall plug to x-ray radiation), and have several applications in the areas of Inertial Confinement Fusion (ICF) and High Energy Density Physics (HEDP) [1]. Z-pinch x-ray sources can be used to indirectly drive HEDP experiments or ICF capsules [2] in a similar manner to the laser experiments that are expected to demonstrate laboratory ignition on the National Ignition Facility. The magnetic pressure generated by large, pulsed currents can also be used to directly compress cylindrical liners containing fuel to the extreme conditions required for fusion [3]. For example, 25 MA at a radius of 1 mm is 100 megabars of magnetic pressure, comparable to the radiation-driven ablation pressure on capsules designed for the National Ignition Facility. Unlike capsule implosions, in which the force driving the implosion decreases with decreasing capsule surface area, the $J \times B$ force increases as current reaches smaller radii and multi-gigabar pressures are possible at radii ~100 μm . The efficient production of x-rays or the direct use of magnetic pressure to drive initially solid metal tubes (liners) relies on compressing matter and current to small radii to create extreme conditions in the laboratory.

In 2009 the Pulsed Power ICF program at Sandia was developing a concept known as Magnetized Liner Inertial Fusion (MagLIF) [3], shown schematically in Figure 1. Previously, cylindrical compression geometries for ICF were considered to be a decisive disadvantage: it would require a larger target convergence to compress DT fusion fuel to high density in this geometry relative to a spherical geometry. However, the MagLIF concept takes advantage of the cylindrical geometry to achieve fusion with relaxed requirements. Our interest in this new approach to fusion was the main driver for this LDRD proposal.

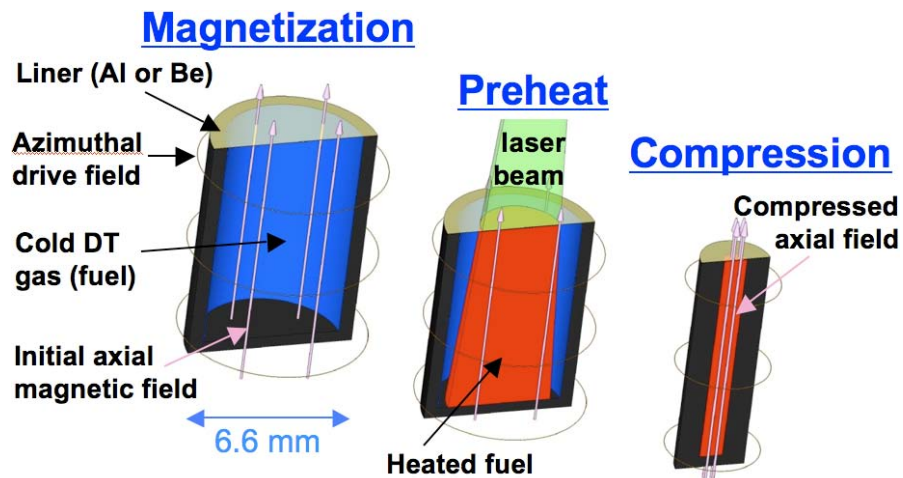


Figure 1: An approach to ICF using the magnetically driven compression of cylindrical metal liners containing magnetized and preheated fusion fuel to the conditions needed for fusion. First, the target containing cold DT gas is magnetized with an axial magnetic field using external field coils (not shown). A laser pulse subsequently heats the fuel to ~250 eV. A current driven through the cylinder produces an azimuthal magnetic field that implodes the shell, compressing the plasma to fusion conditions.

MagLIF target designs have an outer cylindrical metal liner containing the DT fuel and an embedded axial magnetic field (magnetization). With the combination of laser preheating of the fuel and flux compression in the magnetized fuel, multi-keV temperatures can be obtained at stagnation because the DT is put on a higher adiabat and the field insulates against radial thermal conduction losses. Furthermore, the compressed axial field radially confines the alpha particles produced by the DT reaction, allowing them to more easily deposit their energy into the fuel. Unlike spherical capsule implosions on the National Ignition Facility, precise control of the converging shocks is not required to achieve fusion breakeven. The combination of fuel pre-heat and magnetization may significantly ease the difficulty of achieving fusion conditions, lowering the implosion velocity requirement from ~ 350 km/s to ~ 100 km/s and the fuel convergence ratio requirement from $\sim 35:1$ to $\sim 20:1$. The strong magnetic fields created at stagnation may lower the density-radius product of the fuel from ~ 300 mg/cm² to 10-30 mg/cm².

The most important factor limiting the controlled compression of dense matter to small radii using magnetic pressure is the magneto-Rayleigh-Taylor (MRT) instability [4]. In cylindrical liner implosions the MRT instability arises at the outer plasma-vacuum interface, where the driving magnetic pressure plays a role analogous to a light fluid pushing on a heavy fluid (the plasma liner) as in the classical fluid Rayleigh-Taylor instability. The MRT instability is considerably more complex in part because the driving current is not confined to the surface boundary but diffuses into the liner, allowing resistive heating of the liner and distributing the magnetic pressure. This complexity means that we rely heavily on advanced radiation-hydrodynamics simulation tools that incorporate magneto-hydrodynamic physics (e.g., LASNEX, HYDRA, GORGON) to model any z-pinch system.

Surprisingly, at the start of this project there was very little data in the published literature that could be used to validate these simulation tools, particularly in the ~ 100 ns regime. The highest-quality published data on the MRT instability was collected on multi-microsecond time scales [5], where the liner remains in a liquid or solid state for much of the implosion and material strength effects are important. At the shorter time scales of interest here, the liner typically becomes plasma unless the magnetic drive is carefully tailored to avoid creating shocks in the material. Thus, the main thrust of this LDRD proposal was to study the key physics issue of liner stability. These experiments were extremely successful and resulted in several high-profile publications [6,7,8,9,10,11,12]. The results of these studies are summarized in Section 2.

Essential to actually testing the MagLIF concept on the Sandia Z facility is the development of a magnetic field capability. Such field coils are also expected to be useful for fundamental liner stability experiments (strong embedded fields can potentially stabilize the implosion against the MRT instability). This was a significant portion of this LDRD project that we thought would be completed in time for Z experiments in FY2012. A prototype field coil was successfully demonstrated in a new Systems Integration and Testing Facility constructed in part to support this work. Plans and construction are underway for implementing the field coils on Z, with the first tests using this capability expected in the first quarter of CY2013. The coil development and engineering effort are summarized in Section 3.

Finally, the modeling effort for magnetized liner implosions continued under this LDRD. The LDRD supported the publication of the main paper describing the MagLIF concept [3]. In

addition, an advanced version of the concept was developed as part of this LDRD that is capable of high yield and high gain [13]. High-yield targets are a key part of meeting the testing requirements for various National Nuclear Security Administration missions, and high-gain targets would be an essential need for any future inertial fusion energy systems. While the initial calculations were done using the mature LASNEX code, we continued to improve our modeling capabilities with the HYDRA code. HYDRA has a number of advantages including the ability to run 3-D calculations on multiple parallel processors. Calculations done as part of this LDRD substantially advanced the state-of-the-art in modeling these complex problems. We note that while our work within the LDRD was done in the specific context of MagLIF, the idea of relaxing fusion requirements through magnetized and preheated fuel can be applied to many different inertial confinement fusion platforms (e.g., radiation-driven spherical capsule implosions). The results of the modeling work are summarized in Section 4.

This LDRD project was extremely successful in accomplishing most of its goals. Key indicators of this success from the broader ICF and HEDP community include the large number of publications, invited talks, and awards that this project contributed significantly to. These include a Presidential Early Career Award for Scientists and Engineers (PECASE) and a 5-year, \$2.5 million DOE Early Career Research Grant for the principal investigator on the general topic of studying instabilities in imploding liner systems. These accomplishments are summarized in Section 5.

2. LINER STABILITY EXPERIMENTS ON Z

2.1 Overview of Z experiments

The first five Z experiments studying the growth of the magneto-Rayleigh-Taylor (MRT) instability in cylindrical Al liners were launched around the time of the LDRD proposal, and occurred three months before the start of this LDRD project funding. The LDRD project supported the detailed analysis of this data, and the planning and execution of an additional 30 Z experiments over the course of the three years of funding.

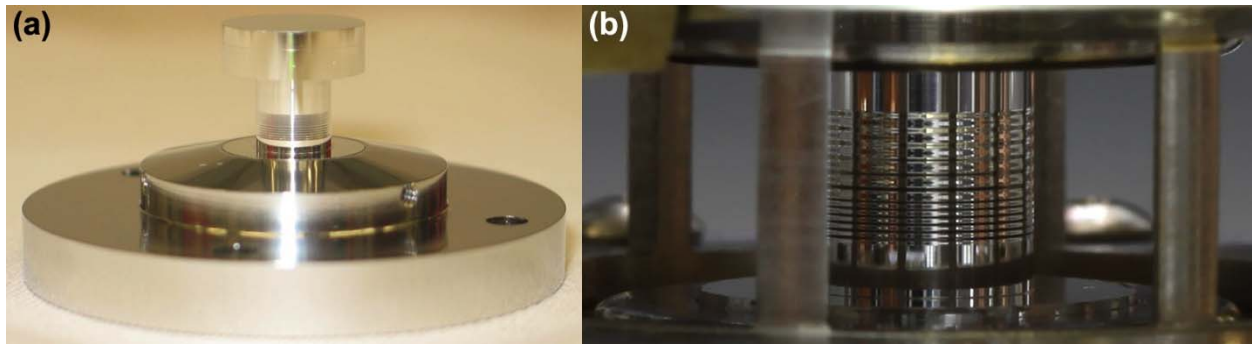


Figure 2: Photographs of Al targets fabricated for use in the initial magneto-Rayleigh-Taylor experiments. The diameter of the targets shown is 0.25 inches (6.35 mm).

Our ability to execute useful liner stability experiments on Z was due to the timely confluence of new target fabrication, diagnostic, and hardware capabilities. When the idea for MagLIF was first conceived the Sandia ICF program began working with General Atomics to develop the capability to make high quality, well-characterized cylindrical aluminum targets with excellent surface finish on site at Sandia. After the start of the LDRD, General Atomics was able to further develop these techniques to fabricate beryllium liners in La Jolla, CA. (A notable accomplishment because beryllium is particularly hazardous to machine and is also very difficult to machine because of its high strength.) Example liner targets are shown in Figure 2. On the diagnostic side, monochromatic 6.151 keV backlighting diagnostics [14] had been continuously developed and improved over the preceding several years [15,16,17]. One or two high-resolution (10-15 μm) radiographs per experiment could be reliably obtained over a large target field of view (up to 4x20 mm). This hardware is illustrated in Figure 3. Finally, the experience garnered from early experiments on the refurbished Z facility was used to design a reliable power-feed hardware set to deliver current to the liner target.

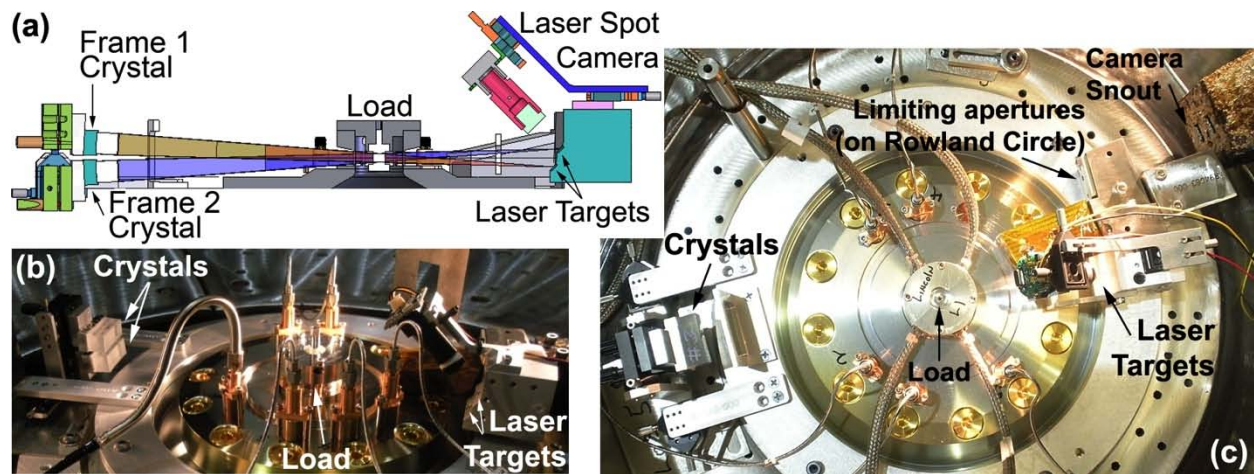


Figure 3: Illustrations of the 2-frame 6.151 keV x-ray backlighting diagnostic for the Z facility. (a) Side-on half-section diagram of the 2-frame backlighter that illustrates the ± 3 -degree view through the load above/below the horizontal. (b) Side-on-photograph of the diagnostic as installed on Z. (c) Top-down photograph of the diagnostic as installed on Z.

A total of 35 Z experiments collected data relevant to the study of liner stability and were supported at least partially by this LDRD. These are summarized in Table 1, and represent a variety of primary goals. Section 2.2 contains a description of the first set of experiments, which examined the growth of single-wavelength MRT modes. This was done by machining small-amplitude, single-wavelength perturbations in the surface of Al liners and measuring the resulting MRT growth using radiography. Section 2.3 describes the next set of experiments, which studied the growth of MRT instabilities in Be liners made using the best available surface finish. The use of Be (which has a much lower opacity at 6.151 keV) allowed us to take penetrating radiographs and study the three-dimensional evolution of the random MRT instabilities that grew. Section 2.4 briefly describes recent improvements on the beryllium radiography experiments, which used thin Al sleeves (of much higher opacity) to provide a high-contrast image of the inner liner surface relative to the MRT-unstable outer surface of the liner. Section 2.5 briefly describes recent attempts to modify the growth of the MRT instability by changing the characteristics of the initial surface finish of the beryllium liner. Finally, Section 2.6 describes experiments whose primary goal was not as liner stability studies, but rather the study of the dynamic material properties of Be and Al. These experiments directly studied the shock launched in the liner when the standard Z current pulse was used, and also the case where the Z current pulse was carefully crafted to avoid launching a shock in the material. The latter technique may have implications as a method for reducing the MRT growth.

This was a three-year LDRD project and was funded as Project 141537 for a total cost of about \$2,900,000 for fiscal years 2010-2012.

Table 1: Summary of the 35 Z experiments to date relevant to liner stability studies. The campaign names relate to the primary goals of the experiments. The AR refers to the liner aspect ratio, defined as the outer liner diameter divided by its thickness. The MagLIF point designs assume a liner with AR=6, but a broad range of ARs may work.

Shot	Campaign	Primary Emphasis	Liner	AR	Radiographs
1962	Lincoln 1	Single-mode MRT	Al	10	1 (out of 2)
1963	Lincoln 1	Single-mode MRT	Al	10	2
1964	Lincoln 1	Single-mode MRT	Al	10	1 (out of 2)
1965	Lincoln 1	Single-mode MRT	Al	10	2
1968	Lincoln 1	Single-mode MRT	Al	10	2
2058	Lincoln 2	Multi-mode MRT	Be	4	0 (out of 2)
2060	Lincoln 2	Multi-mode MRT	Be	4	2
2062	Lincoln 2	Single-mode MRT	Al	10	1
2064	Lincoln 2	Single-mode MRT	Al	10	1
2102	Lincoln 2	Single-mode MRT	Al	10	1
2104	Union 1	Shock measurement	Be	4	2
2105	Lincoln 3	Multi-mode MRT	Be	6	2
2106	Lincoln 3	Multi-mode MRT	Be	6	2
2107	Lincoln 3	Multi-mode MRT	Be	6	0 (out of 2)
2108	Union 1	Shockless compression	Be	4	2
2110	Union 1	Shockless compression	Be	4	2
2172	Lincoln 4	High-CR multi-mode MRT	Be	6	2
2173	Lincoln 4	High-CR multi-mode MRT	Be	6	2
2174	Lincoln 4	High-CR multi-mode MRT	Be	6	2
2207	Union 2	Shockless compression	Be	3.2	2
2208	Union 2	Shockless compression	Be	3.2	2
2209	Union 2	Shockless compression	Be	3.2	2
2210	Union 2	Shockless compression	Be	3.2	2
2250	Union 2	Shock measurement	Be	4	2
2318	Washington 1	Multi-mode MRT enhanced contrast	Be	6	2
2319	Washington 1	Multi-mode MRT enhanced contrast	Be	6	2
2320	Washington 1	Multi-mode MRT enhanced contrast	Be	6	2
2356	Lincoln 6	Surface roughness impact	Be	6	2
2358	Lincoln 6	Surface roughness impact	Be	6	0 (out of 2)
2360	Lincoln 6	Surface roughness impact	Be	6	2
2370	Union 3	Shockless compression	Al	8.9	2
2390	Lincoln 7	High-CR multi-mode MRT (E.C.)	Be	6	2
2394	Lincoln 7	High-CR multi-mode MRT (E.C.)	Be	6	2
2396	Lincoln 7	High-CR multi-mode MRT (E.C.)	Be	6	2
2408	Union 3	Shockless compression	Al	5	2

2.2 Single-mode Magneto-Rayleigh-Taylor experiments

As noted in Section 1, one of the biggest concerns with the MagLIF concept at the time it was proposed was whether the calculations of the MRT growth had any validity. At the time of the experiments, there was surprisingly little data in the published literature that could be used to benchmark our calculations. The only sub-microsecond data we found was from wire-array tests using wires with axial modulations in the initial mass per unit length [18]. Liners composed of an azimuthally continuous, cylindrical tube initiate and evolve differently than liners composed of individual 5-30 μm diameter wires spaced 0.2-2 mm apart azimuthally. Wire-array implosions are dominated by the ablation of about half the initial mass into the array interior before the implosion begins, a consequence of the large skin depth of the current and the small diameter of the wires. By contrast, the thickness of the cylindrical tube liners proposed for MagLIF exceeds the skin depth of the ~ 100 ns current pulse, and no significant prefilling of the interior volume is expected. The remaining published controlled studies of MRT growth were done on multi-microsecond generators in which the imploding liners have significant material strength and remain in liquid or solid states for much of the implosion [5]. By contrast, in fast (~ 100 ns) implosions strong shocks can develop in the liner and the liner is typically in the plasma state for much of the implosion.

In the absence of data, it was not clear whether the predictions of LASNEX and other codes were correct, particularly when the codes gave different predictions for the same problems. To obtain data for validating the simulation predictions, the first set of experiments were designed to measure the growth of single-wavelength modes of MRT. To seed these modes, we machined small-amplitude, sinusoidal perturbations into the surface of the liner, as shown in Figure 2. The growth and amplitude of these perturbations as a function of time was measured using the 6.151 keV radiography diagnostic described in Figure 3. Example radiography data from these experiments is shown in Figure 4. These images show a number of unique features that were compared to simulations, such as the unique jets visible at time 5 in the 200- μm -wavelength portion of Figure 4.

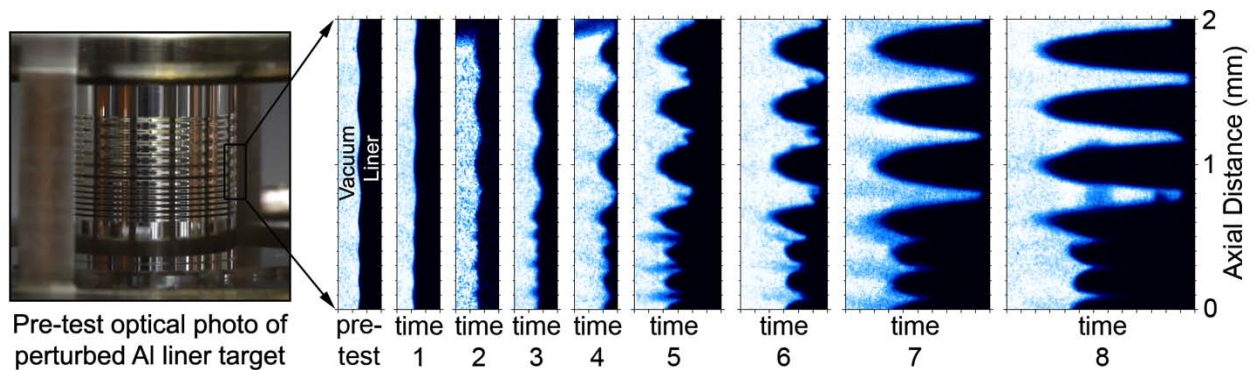


Figure 4: Hollow cylinders of aluminum (liners) were imploded on the Z machine during the first set of MRT experiments. Sinusoidal perturbations with wavelengths of 200 and 400 μm (and peak-to-valley amplitudes of 10 and 20 μm , respectively) were machined onto the outside surface of the liner, as shown in the photograph. This deformation was captured using x-ray radiography at 8 different times during the implosion as shown.

The radiography data were compared with pre-shot LASNEX simulations, and the agreement was surprisingly good. For example, the plasma jets were seen in our pre-shot LASNEX simulations, but there were varying opinions at the time as to whether the jets were real or if they were a numerical artifact. The amplitude of the 400- μm -wavelength mode as a function of time was compared with the simulations as well, as shown in the plot in Figure 5.

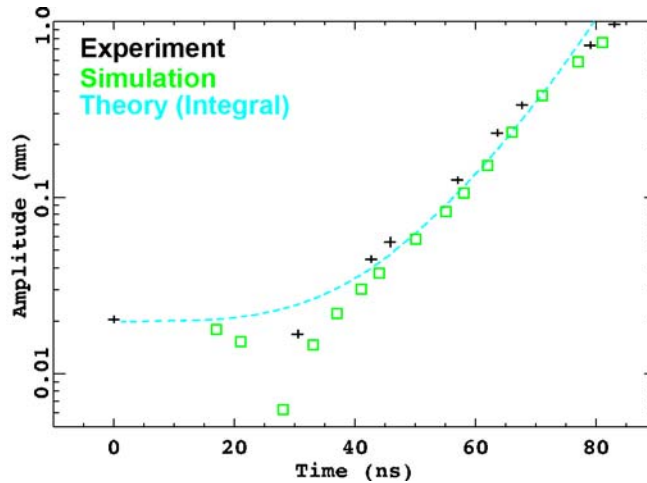


Figure 5: Analysis of the 400- μm wavelength data from Figure 4. The peak-to-valley amplitude from experiments (black) is compared to simulations (Green) and analytic theory (blue). The decrease in amplitude between 18 and 40 ns is caused by plasma ablating from the liner surface.

Additional data along with far more detailed comparisons between the simulations and experiments are described in two of our publications [6,7]. Comparisons between these data and several simulation tools used in the ICF and HEDP complex are ongoing, including LASNEX, GORGON, ALEGRA, HYDRA, KULL, and ARES. These data are proving to be a key benchmark for validating the predictions of these complex radiation-MHD simulations.

2.3 Beryllium liner experiments studying multi-mode MRT growth

After the initial success at modeling single-wavelength modes of the MRT instability starting from well-defined, pre-seeded conditions, we began examining multi-mode MRT growth. For these experiments we chose to use beryllium liners, which because of the low opacity of Be to 6.151 keV photons, allowed us to take fully-penetrating radiographs through the entire volume of the liner during most of its implosion. Rather than seeding a particular wavelength of MRT, the liners were machined to be “smooth” with the best available surface finish. The dimensions and aspect ratio of the liners were chosen to be the same as the nominal point design for the MagLIF concept ($r_{\text{outer}}=3.47$ mm, $r_{\text{inner}}=2.89$ mm, $AR=6$). Radiographs were taken at a variety of times during the implosion and compared with our simulations. Example data from these experiments are shown in Figure 6, taken from [11].

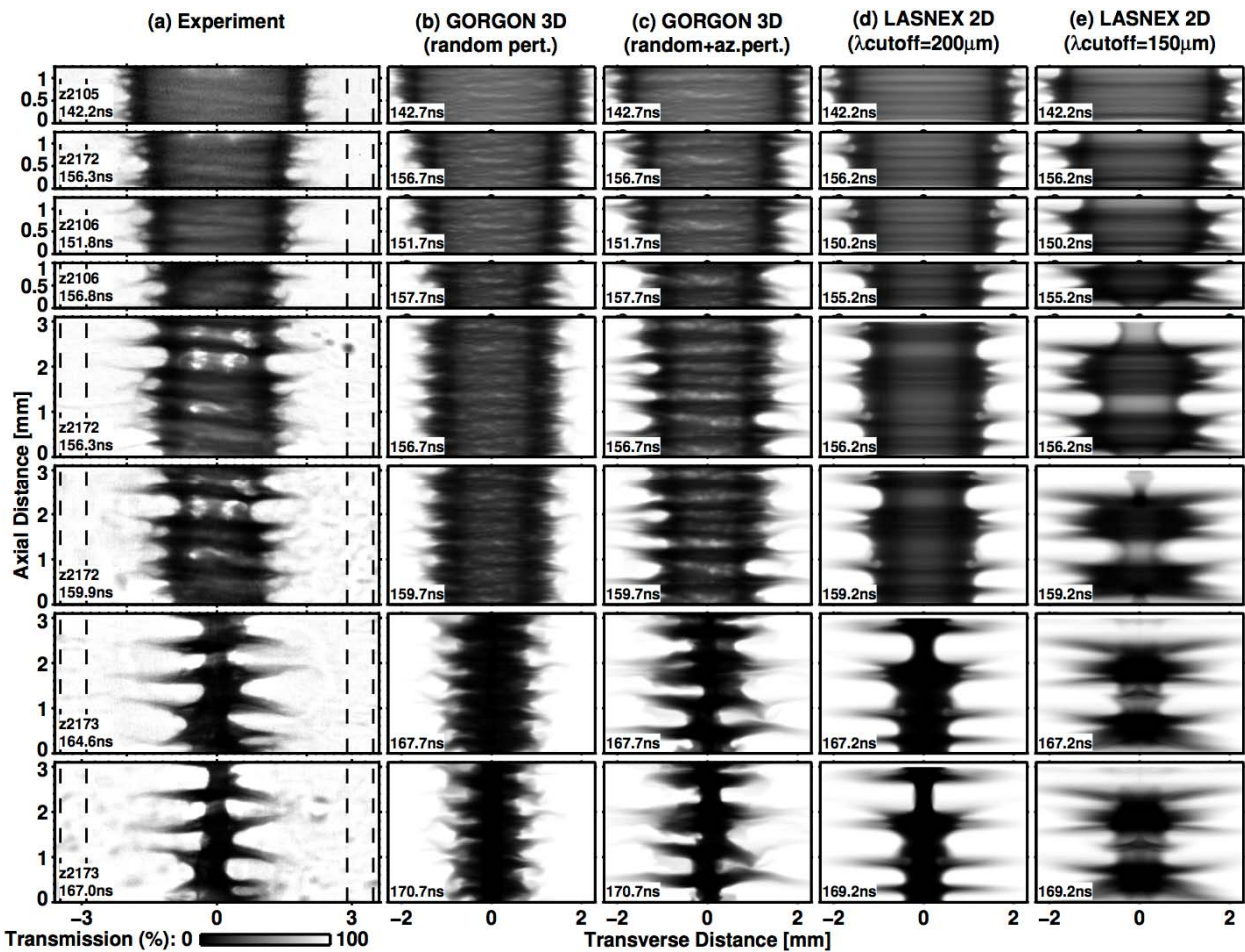


Figure 6: (a) Radiographs of beryllium liner implosions. The latest (bottom) two frames captured the implosion just after the inner liner surface had stagnated on axis and while trailing liner material continued to flow into the stagnation column, compressing the column further. The vertical dashed lines indicate the initial positions of the inner and outer liner surfaces. (b-e) Synthetic radiographs from radiation-MHD simulations using the 3D GORGON code and the 2D LASNEX code.

Obtaining this level of azimuthal correlation from 3D Eulerian radiation magneto-hydrodynamic simulations turned out to be nontrivial, as is illustrated in Figure 6, where we present synthetic radiographs from a pair of simulations that used the 3D GORGON code. The resolution for both of these simulations was $20\ \mu\text{m}$. The simulation in Figure 6b was initialized solely with a white-noise random perturbation applied to the outer surface of the liner (i.e., cells adjacent to the liner’s nominal outer surface were randomly filled with solid Be). Compared to the experiments, this simulation produced significantly less horizontal banding and azimuthal correlation. In an attempt to enhance the azimuthal correlation, and thus to better match the experiment data, the simulation in Figure 6c was initialized with a bias applied to the random-surface generator at several axial locations. This bias was applied to the entire circumference of the cylinder at these locations, and each location was one cell tall. These locations were selected randomly with about 3 occurring every axial mm. This methodology is reasonable in that the surface finishes of the liners used for these experiments did have significant amounts of azimuthally-correlated structure due to the fabrication process, as shown in Figure 7.

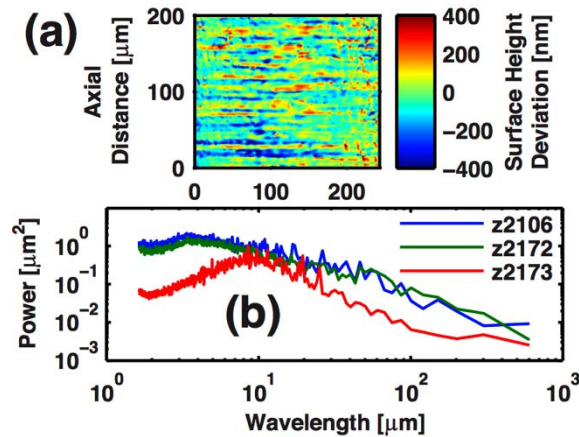


Figure 7: Liner surface finish data. (a) Sample of surface height variation illustrating azimuthally-correlated structure (striations) due to the single-point, diamond-turned fabrication process (the liners were not polished or further modified). (b) Power spectra for axially-aligned wave vectors (600 μm axial sample length). The liner surface finishes had a root-mean-square roughness of 100-250 μm .

We also ran several simulations using the 2D LASNEX radiation magneto-hydrodynamics code. These simulations included a Fourier-series-constructed model of the initial liner surface that was based on a fit to the characterization data shown in Fig. 3(b). Interestingly, we found that the Fourier components with wavelengths less than about $200\ \mu\text{m}$ needed to be excluded from the surface construction, else the MRT structure would grossly overdevelop relative to the experiments (see Figure 6d-e). We believe this is because all perturbations in 2D simulations are by definition perfectly correlated azimuthally. In an experiment, however, the azimuthal correlation lengths of very short wavelength perturbations are small compared to the liner circumference, and thus these very short wavelength perturbations cannot contribute to the MRT development as much as that predicted by a pure 2D simulation.

More detailed analysis and comparisons to simulations can be found in [11]. Like the initial experiments described in Section 2.2, these data are being used to validate simulations from a wide variety of radiation-MHD codes.

2.4 Enhanced-contrast beryllium liner experiments using Al sleeves

While the radiography data shown in Figure 6 has been extremely valuable, it can be difficult to unambiguously discern the position of the inner liner surface, particularly at high convergence (late times). This is because the modulations of the outside surface induced by the MRT growth interferes with the ability to see the inner surface, particularly when the modulations are clearly in violation of the cylindrical symmetry assumption needed to do an accurate Abel inversion for reconstructing the radial density profile.

To improve upon the results shown in Figure 6, new target assemblies were developed. The same beryllium liners with $AR=6$ were used as before, but an additional 2- μm thick Al sleeve was inserted just within and adjacent to the Be liner's initial inner radius. The low mass and thin radial extent of this sleeve results in a negligible perturbation to the overall liner implosion. However, the opacity of the Al at 6.151 keV is considerably higher than that of Be. Thus, the position of the Al sleeve is easy to pick out in 6.151 keV radiographs of the liner implosion, providing an "enhanced contrast" image of the stability of the inner liner surface. The radiographs obtained to date using this method are shown in Figure 8. It is clear from these images that the inner liner surface remains remarkably unperturbed relative to the strong modulations growing up on the outside of the liner. This experimental data provides a strong confirmation of the predictions of the original MagLIF paper [3], which suggested that a relatively thick liner with a low aspect ratio (e.g., 6) would retain a reasonably stable interior with enough areal density to inertially confine the fusion fuel. To put the data in Figure 8 in perspective, the opaque on-axis rod used in the bottom three radiographs is about the diameter that the MagLIF plasma needs to reach in order for us to achieve ~ 100 kJ DT yields on Z. These data are therefore very encouraging.

The analysis of these data is currently underway. We expect to publish these images and the corresponding analysis in a Physics of Plasmas article to be submitted in November 2012 as part of an invited talk by Ryan McBride at the APS-DPP meeting [12].

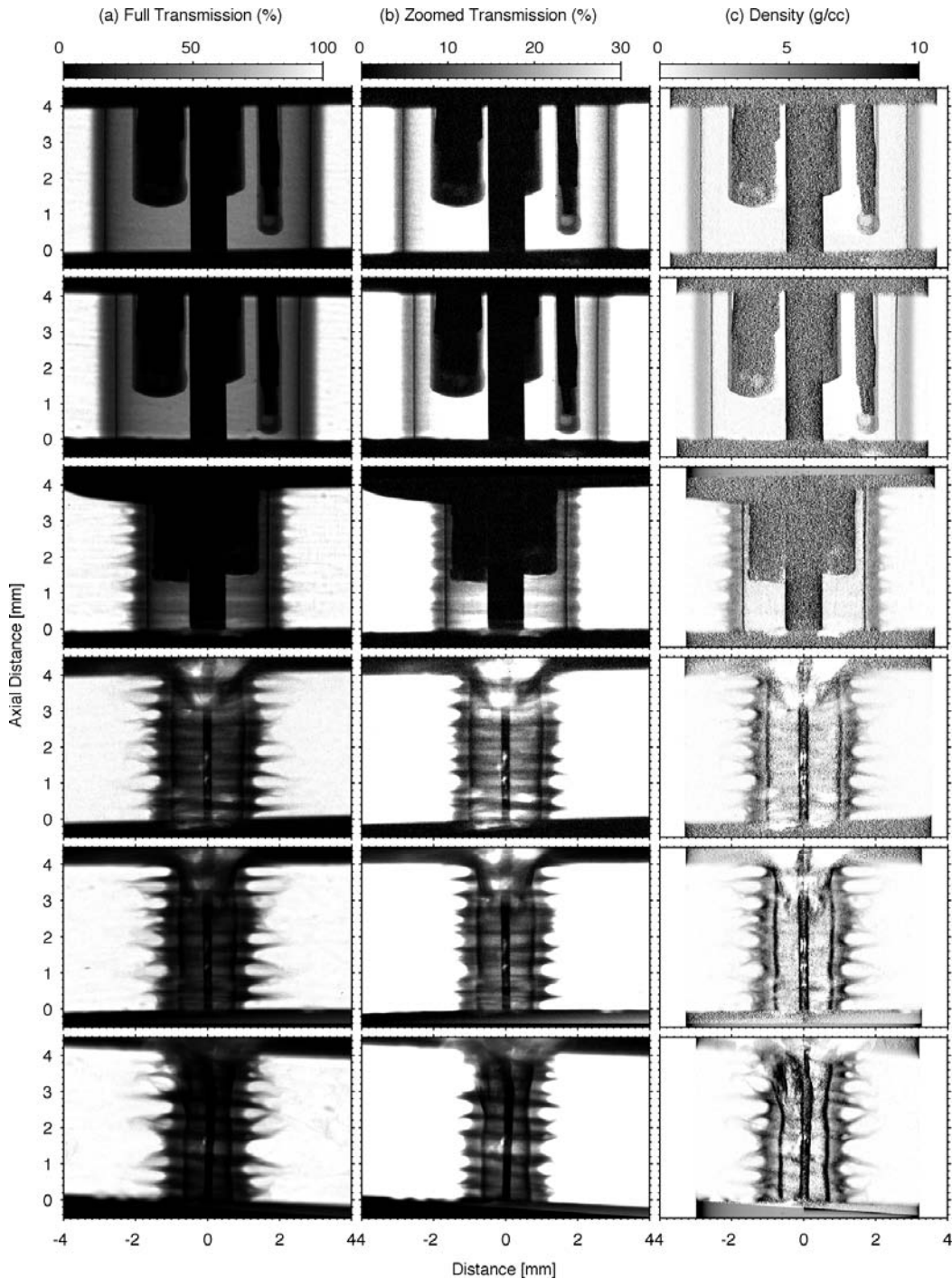


Figure 8: Analysis of radiography data designed to enhance the contrast of the inner liner surface. The experiments shown used AR=6 beryllium liners with a 2- μ m thick Al sleeve inserted just inside the inside surface of the beryllium. (a) The radiograph images in transmission units. (b) The same radiographs with the color range remapped to the 0-30% transmission to enhance the visibility of low-transmission features. (c) Density contour plots obtained from Abel transforms of the transmission data assuming cylindrical symmetry. These are only valid outside of the Al sleeve position. The interior structures seen in the top three radiographs are micro-B-dot probes used to measure the flux inside of the liner at early times.

2.5 Experiments studying role of surface roughness on MRT growth

One of the key questions raised by the data and simulations discussed in Section 2.3 is whether we can affect the growth and correlation of the magneto-Rayleigh-Taylor instability by altering the initial surface finish of the liner. For example, comparing the two sets of GORGON simulations shown in Figure 6b-c, we see dramatic differences in the late-time structure of the two liner implosions depending on how the surface roughness of the liner is treated. If it is assumed that some level of initial correlation is present along the azimuthal direction, then the late-time structure of the liner has substantial azimuthal correlation, even though the amplitude of the initial correlation was very small. By contrast, if there is no azimuthal correlation and the surface perturbations are random, then the growth of the MRT appears to be slower, as in Figure 6b.

As shown in Figure 7, the liners are known to have structure that is highly correlated along the azimuthal direction because of the way the liners are machined. The cylinders are diamond-turned on a lathe, which leaves a very specific pattern on the liner surface that depends on both the shape of the tool tip and the axial feed and rotation rates. Detailed analysis of the surface finish confirms the predicted model for what this shape should look like. If the liners were machined or treated in a different way, would it be possible to dramatically change the late-time structure to look more like the results of Figure 6b?

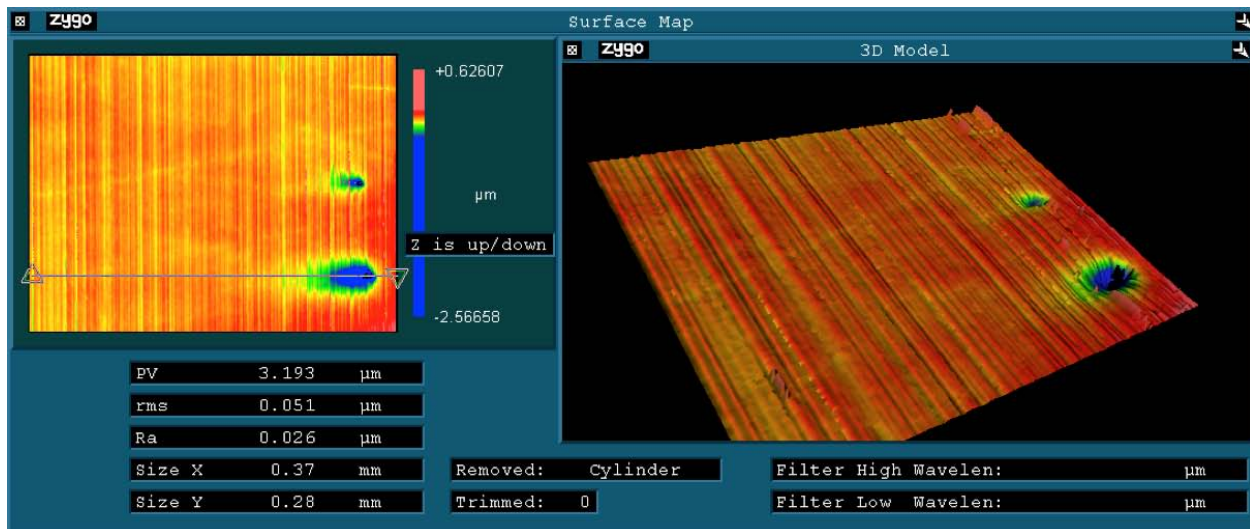


Figure 9: Example surface characterization data collected with a Zygo interferometer. On the left side a 2D color contour plot of the depth of the surface is shown, with the axial direction of the cylinder along the vertical direction. On the right side a 3D rendering of the same data is shown. Unlike the data in Figure 7, there is no consistent azimuthal correlation of the surface structure.



Figure 10: Photo of an axially polished beryllium cylinder.

A very recent series of shots on the Z facility in May 2012 attempted to address this issue. For these experiments, the same beryllium liners were fabricated as in Section 2.3. The key difference was that after the liners were machined in the usual way, which left azimuthally-correlated machining tool marks, the liners were polished. A fine grit was applied to the surface of the liners and a polishing rag was run across the surface of the liner only along the axial direction. The result was not only an improvement in the overall surface roughness of the liner down to about $50\ \mu\text{m}$, but also the complete elimination of the azimuthally-correlated tool marks in favor of an axially-correlated surface finish. Since the growth rate of MRT instabilities in the r-theta plane is negligible compared to that in the r-z plane, this is predicted to dramatically alter the resulting MRT growth. An example liner body fabricated and polished in this way is shown in Figure 10.

These liners were fielded in a set of three experiments in May 2012 (z2356, z2358, and z2360). Unfortunately, as indicated in Table 1, no radiographs were obtained on z2358 due to a problem with the T1 triggering system that fires the Z-Beamlet laser on Z shots. The radiographs from the other two experiments are shown in Figure 11. The goal was to obtain data at times similar to those from Figure 6. The relative timing of the radiographs obtained with respect to those from previous experiments is shown in Figure 12. The late-time radiographs from z2356 were very near the radiograph times from z2172 in Figure 6.

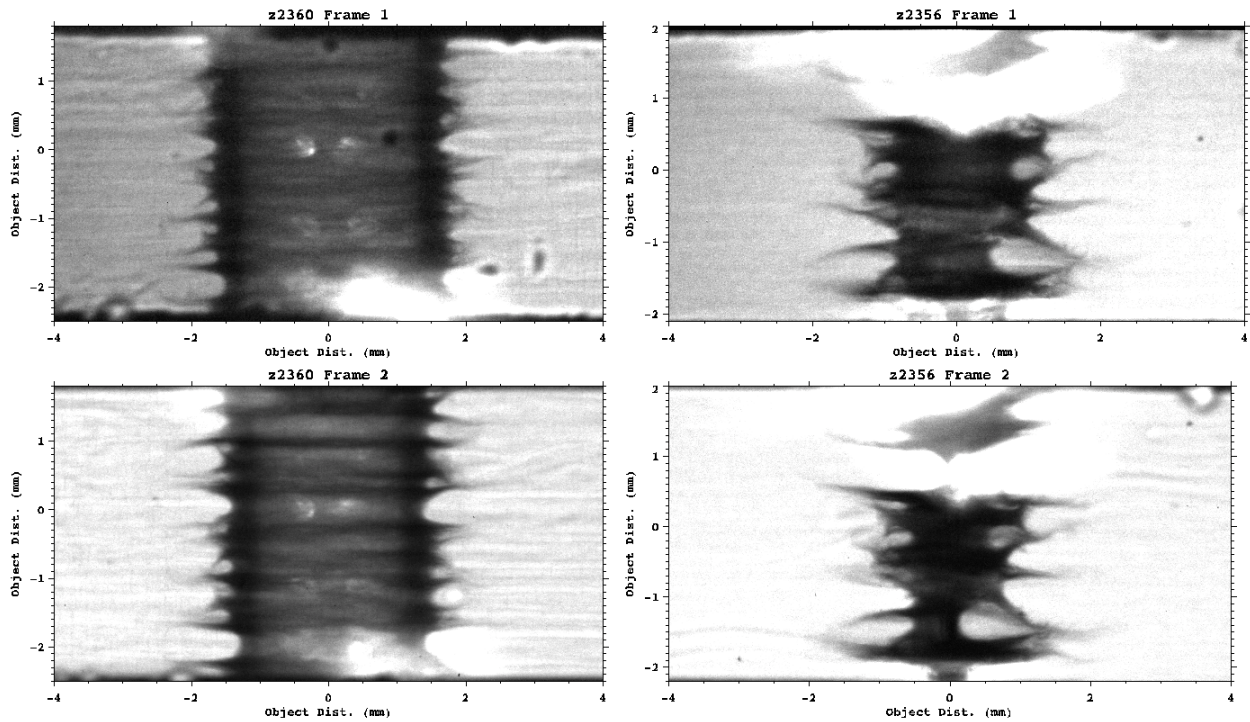


Figure 11: Radiographs from shots examining the impact of surface roughness on the growth and correlation of the MRT instability.

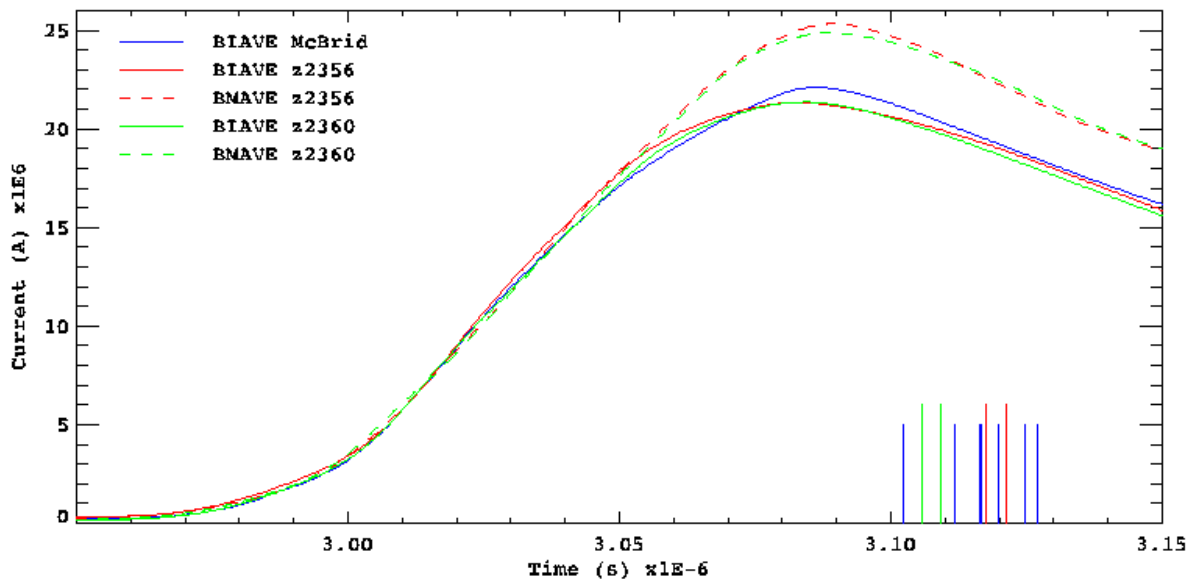


Figure 12: Timing of the radiographs with respect to the current pulse. The radiography data from Figure 6 were obtained at the times indicated by vertical blue lines. The radiography data from Figure 11 were obtained at the times indicated by vertical red and green lines.

A detailed analysis of this data is still pending at this time. A preliminary comparison of the z2360 frame 2 data from Figure 11 with the z2105 frame 2 data from Figure 6, taken at an

equivalent time, suggests that the structure is very similar in amplitude, wavelength, and level of azimuthal correlation. By contrast, the z2356 radiographs are within 1 ns of the equivalent time of the z2172 radiographs from Figure 6, and yet they appear to show much less azimuthal correlation and structure compared to the z2172 data. Since the difference between the two GORGON simulations at the earlier times are subtle while the late-time differences are more dramatic, this difference between the two sets of experimental data may imply that we have succeeded in altering the late-time structure of the MRT instabilities on the liner.

To make this conclusion more compelling, more radiography data will be needed. One additional liner target and hardware set exists, but was unable to be fielded in May due to conflicts with a higher-priority experiment on Z. The remaining target will be fielded during October 2012, with the goal of obtaining radiographs at a time intermediate with the radiographs in Figure 11.

2.6 On the possibility of current pulse shaping to improve stability

The standard, rapidly rising Z current pulse (e.g., see Figure 12) will create a magnetic pressure that launches a strong shock in the bulk liner material. The shock is strong enough to melt the liner material, so that when the liner begins to implode it is a shell of molten metal. The shocked material is also at a higher density, and density discontinuity at the shock position can be directly observed using radiography. Example radiography data illustrating the density jump is shown in Figure 13. The discontinuity is easier to see in axially-averaged lineouts along the radial direction. Lineouts from four different radiographs are shown in Figure 14a that show the propagation of the shock through the bulk material, before it reaches the inner liner surface.

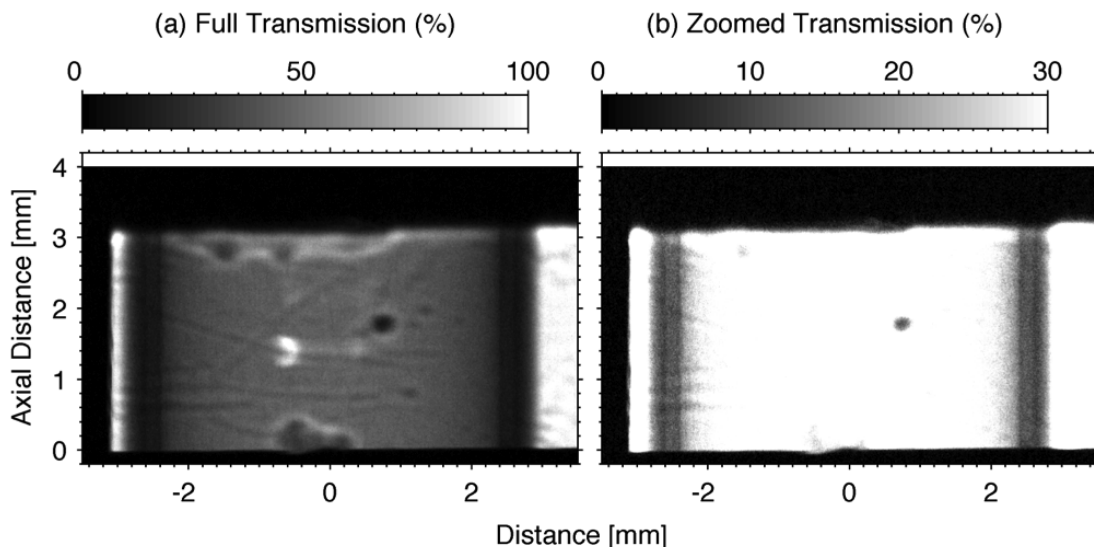


Figure 13: Example radiograph from z2104 showing a sharp discontinuity in the density (opacity) of the liner due to a strong shock. The image on the left is shown from 0 to 100% transmission. In the left image the color scale was remapped to display the 0-30% transmission range in order to see the low-transmission regions more clearly.

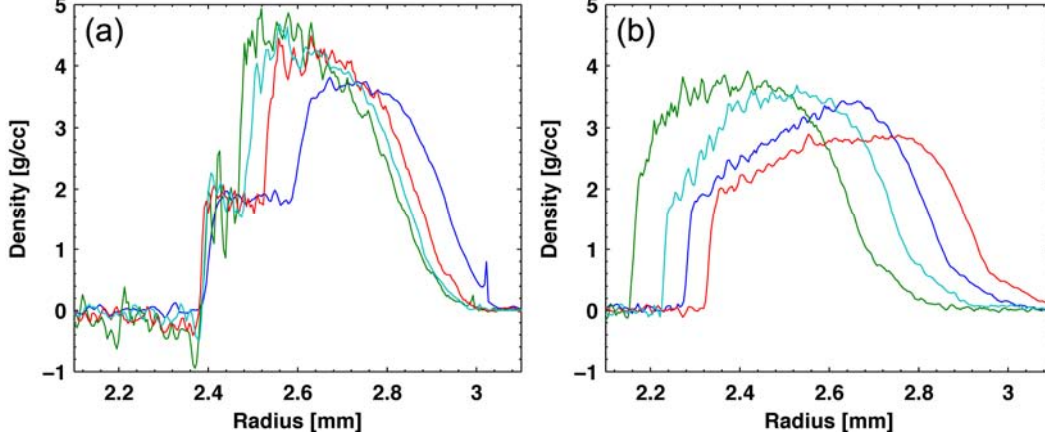


Figure 14: Axially averaged lineouts from radiographs of experiments (a) in which a strong shocked was launched, and (b) in which the current pulse was shaped specifically to avoid launching a shock in the liner. In both cases an AR=4 beryllium liner was used.

As part of this LDRD, we began examining whether it is possible to reduce the amplitude of MRT instability growth in imploding solid liners by “shockless” acceleration. By carefully tailoring the magnetic pressure history on the liner, it is possible to keep a portion of the liner in the solid state for much of the implosion. The main limit to this technique is that the magnetic flux slowly diffuses into the liner from the outside and the material is then resistively heated above the melting temperature. It is conjectured that a liner that remains mostly solid during the implosion will have a smaller MRT modulation in its areal density compared to a liner that is shocked and melted.

To understand why, we consider the linear growth rate γ_e of the MRT instability in a solid material with shear strength G . In [19] it is shown that

$$\gamma_e = \sqrt{Aka - (1 + A)Gk^2\rho}, \quad (1)$$

where A is related to the density of materials on opposite sides of the accelerating interface, $A=1$ in the case of solid/vacuum, k is the wave number, ρ is the liner density, and a is the magnetic acceleration. It is evident from Eq. (1) that the growth rate of the MRT instability is reduced in an accelerating material with strength. Furthermore, shear waves provide a restoring force that stabilize MRT modes with wave lengths less than [20]

$$\lambda_c = \frac{2\pi G}{Aa\rho}. \quad (2)$$

According to Eq. (2), if $G/a\rho$ is large enough perturbations with wave lengths on the order of the liner thickness can be stabilized [21], which could be accomplished by controlling the time history of the acceleration a .

Experiments on Z have shown that beryllium and aluminum liners can be imploded shocklessly (shockless acceleration) by controlling the rise time of the magnetic pressure drive (i.e., the acceleration a), which keeps a fraction of the material in a solid state and maintains its strength.

Thus, according to the linear theory, shockless acceleration may be a way to reduce MRT growth in solid liner, z-pinch implosions.

Shockless acceleration is accomplished by forcing the magnetic pressure to increase with time in a manner that precludes hydrodynamic pressure waves with different characteristic velocities from converging at a point in the material and forming a shock. In this case the acceleration is almost isentropic, with a small increase in entropy and material temperature (~ 100 K) due to inelastic processes; not enough to melt the material.

Key differences in the state of the liner material produced by magnetic acceleration with and without shock formation are illustrated using experimental and simulated results of two shots on Z; 2207 and 2104. The liner shocks up during acceleration in 2104; it is shocklessly accelerated in 2207 [10]. Solid liners composed of Be, density $\rho=1.85$ g/cc, coaxial with a 1.3 cm radius anode return current can, also composed of Be, were used in both shots. In 2104 liner specifications were inner radius $R_i=0.239$ cm, outer radius $R_o=0.319$ cm, aspect ratio $AR=4$, and mass per length $m=0.259$ g/cm; in 2207 $R_i=0.20$ cm, $R_o=0.29$ cm, $AR=3.2$, and $m=0.256$ g/cm. Two-dimensional simulations are performed using the multi-dimensional, radiation, magnetohydrodynamics (RMHD) code ALEGRA [22]. In both cases the MRT instability is initiated by a 100 nm perturbation of the outer radius that is random in the z-direction.

Load currents used in these shots, and to energize the simulations, are plotted versus time in Figure 15a; simulated velocities of the liner inner surface vs. time are plotted in Figure 15b. The short pulse mode current used in 2104 drives a shock into the liner, which is evident as a step in velocity at time 3.06×10^{-6} s. In contrast, there is no evidence of shock up in the 2207 liner velocity; the load current for 2207 is designed to accelerate the Be liner shocklessly [10], which was evidently successful.

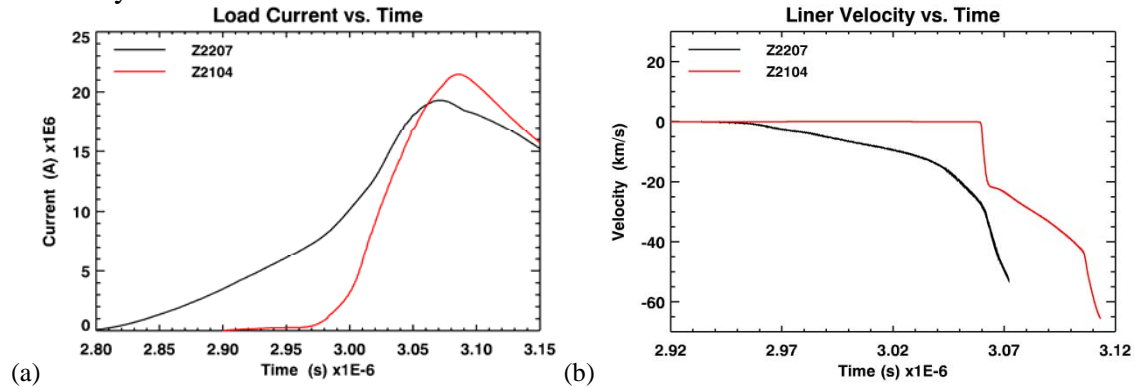
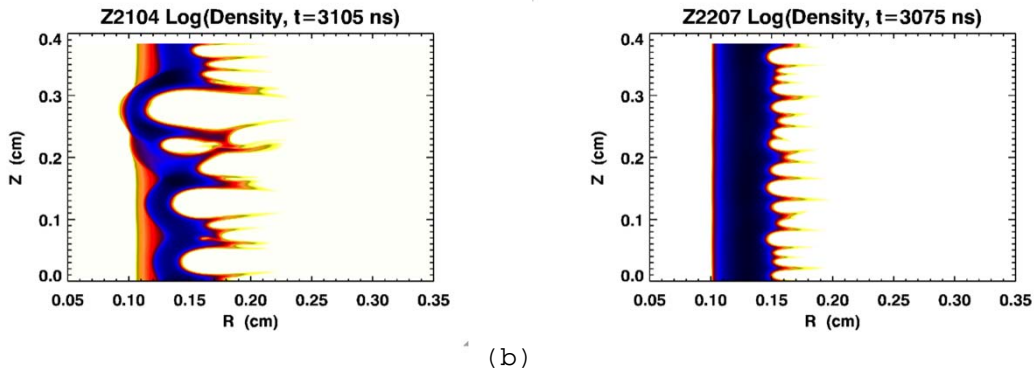


Figure 15: (a) Load current vs. time. (b) Simulated velocity of the liner inner surface vs. time.

Filled contours of simulated liner density are plotted in Figure 16 for both shots, at times when the liner inner surfaces are at approximately the same position. The MRT amplitude is evidently larger in the 2104 liner despite having used identical surface perturbations. This will be discussed further below.



(a) (b)
Figure 16: Filled contours of simulated liner density for (a) z2104, and (b) z2207.

Two x-ray radiographs taken in shot 2104 captured the shock in the liner before it reached the inner surface. The earlier of the two radiographs is shown in Figure 13. The radiographs are Abel inverted to obtain a z-averaged liner density vs. radius. Comparison of Abel inverted densities with results from ALEGRA simulation verifies that the Be liner did indeed shock up, as is shown in Figure 17. The shock is evident as a sharp jump in density relative to the ambient value.

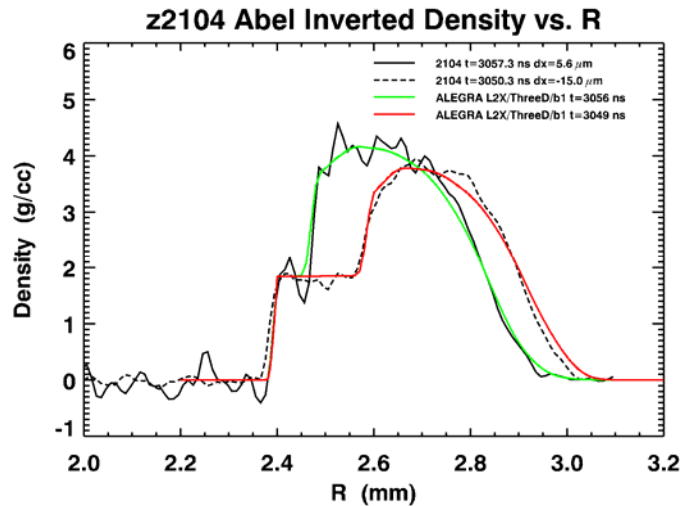


Figure 17: Simulated and measured density vs. position for z2107. Densities at time 3050.3 ns correspond to the radiograph in Figure 13.

ALEGRA simulation verifies that the shock in the z2104 liner attained a peak pressure of about 3.8 Mbar, which heats the material sufficiently to melt it. ALEGRA simulation shows that the liner in z2207 implodes shocklessly, with some fraction of the material remaining in the solid state until stagnation [22]. Figure 18 is a plot of shear strength G vs. time at Lagrangian locations near the liner inner surface. In ALEGRA, when a material melts its shear strength goes to zero; in contrast, the shear strength of a solid increases with time under dynamic compression. Thus, according to Eq. (1) one might expect the growth of the MRT to be reduced in the shocklessly accelerated liner, z2207, relative to the liner in z2104, which seems to be borne out in Figure 16. However, the acceleration time histories for the two liners are quite different; consequently, it is not possible to attribute the larger MRT modulation in the z2104 liner to loss of strength alone.

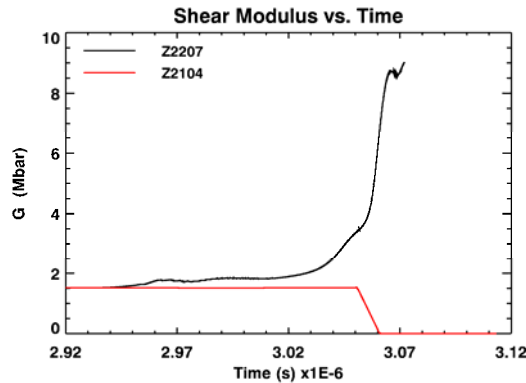


Figure 18: Plot of the shear modulus G vs. time from ALEGRA simulations of z2104 and z2207, which illustrates that in the shockless case (z2207) the liner remains in the solid state with strength.

When the beryllium liner melts its electrical conductivity decreases significantly, which allows the magnetic field to diffuse more rapidly toward the inner surface thereby exacerbating the growth of MRT bubbles. Figure 19 plots simulated electrical conductivity vs. time for the two shots at similar Lagrangian locations. Comparison with Figure 18 shows that when the z2104 liner melts its electrical conductivity decreases by a factor of 26, compared to only a factor of 2.6 decrease in the shocklessly accelerated, z2207 liner (over the entire implosion). Thus, the diffusion rate is about 10 times faster in the z2104 liner, which could lead to larger MRT modulation as seen in Figure 16.

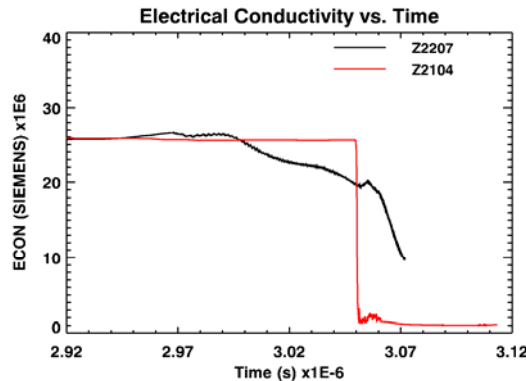


Figure 19: Plot of electrical conductivity vs. time from simulated shots z2104 and z2207.

Results of ALEGRA 2D, radiation-MHD simulations of shots z2104 and z2207, in conjunction with linear theory, suggest that maintaining the liner in a solid state should reduce the amplitude of MRT modulation relative to a liner that implodes as a molten shell. This can be accomplished by shaping the current pulse to shocklessly compress the liner material for the duration of the implosion. Keeping the liner solid maintains its strength, which reduces the linear growth rate of the MRT relative to a melted liner. Furthermore, the electrical conductivity is much larger in a solid metal liner relative to one that melts due to shock heating; larger conductivity reduces the rate at which the magnetic field diffuses toward the inner surface, which could delay the arrival of large MRT modulations at the liner inner surface.

The liners simulated have near identical masses, although the locations are slightly different, and the same surface perturbation is applied. The shocklessly accelerated liner exhibited much less MRT growth when compared at the same radial location. However, since the simulated acceleration histories are not identical it is not possible to conclude definitively that the difference in MRT growth resulted from shockless acceleration vs. acceleration with shock-up; part of the difference could be due to the difference in acceleration. In future work it will be necessary to use optimization techniques to remove the difference in acceleration histories by shaping the current for the shocklessly accelerated liner accordingly.

2.7 The use of pulse-shaped liners for dynamic materials experiments

Once the liner stability experiments supported by this LDRD began, it was recognized that this platform and methodology could be usefully applied to dynamic materials experiments. The traditional geometry for such experiments on Z was planar. Magnetic flux was inserted into the gap between two planes, and used to either drive a flyer plate located on one plane to high velocities for shock experiments, or to shocklessly compress a sample located on one plane. However, the natural geometry for magnetic flux is a cylinder, and in principle it is possible to achieve much higher pressures in a cylindrically convergent geometry than in the divergent planar geometry.

As a proof of principle for this technique, a series of experiments with low-aspect-ratio beryllium liners was fielded (named “Union” in Table 1). Current pulse shapes were carefully calculated using the accepted model for the beryllium equation-of-state, and simulated radiographs of the liners were calculated using ALEGRA simulations using this equation-of-state model. The experiments used radiography images of the liner implosions to infer the radial density profile at several times during the implosion. A detailed, self-consistent method was developed for using the radiography data to infer the pressure and density in the material [9,10], and peak pressures up to 5.5 Mbar were inferred from the data. This pressure is several times what could be achieved in the standard planar geometry [8]. Significantly more detail on this work can be found in these publications [8,9,10].

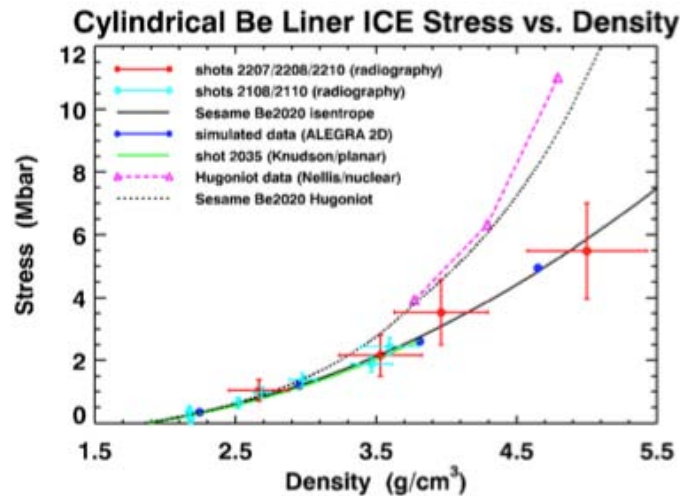


Figure 20: Abel-inverted density profiles at six separate times as determined from experimental radiographs of beryllium liner implosions. Taken from [10].

This LDRD project contributed to the development of the targets, radiography diagnostics, and hardware platform used in these experiments, however, most of the work specific to these experiments was funded by the Dynamic Materials Program at Sandia. We discuss it here because it is evidence of the clear impact of this LDRD on future programmatic work. Also, the radiography data collected in these experiments also provides additional data for benchmarking liner stability calculations, particularly in the context of the discussion of Section 2.6.

3. DEVELOPMENT OF MAGNETIC FIELD SYSTEM

3.1 Introduction

Experiments to test the MagLIF concept [3] are scheduled to begin on Z in CY2013. These experiments will require the integration of three unique elements and capabilities: initial fuel and liner magnetization by a magnetic seed field, fusion fuel preheat by the Z Beamlet laser and fast cylindrical implosion of the liner by the Z current pulse. To fully test the MagLIF concept on will Z require seed magnetic fields of 10 – 30 T (and possibly higher), laser preheat energies of 2 – 8 kJ and peak load currents of 18 – 26 MA. There is also considerable interest in using the magnetic field coils for liner stability experiments, but the requirements for those are less well-defined and depend on exactly how the hypothesis is tested.

The main system requirements, objectives, constraints and assumptions that have driven and influenced the design of the magnetic field system are the following:

1. The seed magnetic field pulse length must be slow enough to achieve the required magnetization without crushing, buckling or deforming the metal liner.
2. Initial experiments must provide full diagnostic access for the 2-frame 6.151 keV backlighter system, the entire suite of soft x-ray diagnostics at 0 and 12 degrees while providing the highest field possible, ideally 10 – 15 T and, in addition, provide access for VISAR load current monitors.
3. The system should minimize the power flow feed inductance required to accommodate the field system to facilitate achieving the highest peak drive currents for the implosion.
4. The system should be consistent with the ability to ultimately achieve fields ≥ 30 T with state-of-the-art coil technology in a system that provides little or no diagnostic access beyond the ability to measure neutron yield.
5. It is assumed that because of the proximity of magnetic field coil system to the load and the energetic nature of a Z experiment that the system will be destroyed on every experiment.
6. Even though the coils are not expected to survive more than one shot, the reliability of the coils should be high enough to guarantee that the desired field is achieved at the time of the Z accelerator pulse.
7. The system on Z should utilize existing capacitor banks.
8. All of the hardware and systems to be fielded on Z should be fully tested and validated prior to delivery or use on Z.
9. The system should be consistent with existing load hardware designs and practice, utilize the standard post-hole convolute system, must be consistent with ES& H protocols and considerate of minimizing impact on Z operations.
10. The system should minimize the induced forces on load and feed hardware and must not deform or affect the delivery of the power flow in an adverse manner.

The development of the magnetic field system for these experiments has been under development for 2 – 3 years. This report describes some key magnet system developments, initial power flow experiments and development of capabilities and facilities that have been supported by this LDRD in preparation for the MagLIF experiments in CY2013. The magnet

system is also intended to support future liner stability experiments. This section is organized as follows. In Section 3.2, we discuss the design and development of the identical capacitor bank systems that will be used in the Systems Integration Test Facility and at the Z facility. In Section 3.3, we give an overview of the roadmap for coil system design and development. In Section 3.4, we describe the design, development, and testing of a 10-T magnetic prototype system. In Section 3.5, we discuss the results of initial power flow experiments with prototype power feeds conducted in March 2012 on Z. In Section 3.6, we discuss the design status of the experimental hardware to be used for the first magnetized experiments on Z.

3.2 Capacitor bank system development

Early on in the MagLIF development project, an existing capacitor bank was identified as the best and least expensive option for repurposing to meet the needs of the MagLIF program. This capacitor bank was purchased in the mid 1990's for use by the ICF program for applied-B ion diode research and by the Radiographic Technologies Program for immersed diode research. This bank consisted of four 4-mF, 15-kV modules (450 kJ per module). A picture of two of the four modules is shown in Figure 21. The four modules were originally purchased to power four individual coils for the extraction diode research program on Sabre. These banks were subsequently adapted to power large, single-coil systems for immersed diode research. It was learned that powering a large coil system with four individual modules was problematic because of difficulties paralleling four systems with individual switches due to timing issues. To solve this problem, a set of isolation diodes and resistors were placed in series with each module. The series resistors are required to limit the current through diodes in the event of a fault. The system was used initially to power immersed diode experiments on Hermes III in 1996 and was used during various immersed diode campaigns until the last experiments were performed on RITS-3 in 2005.



Figure 21: Two capacitor bank modules stacked vertically.

To meet the needs of the MagLIF program, it was decided that it would be best to build two identical banks systems using 2 modules each. One system would be used for development and testing of the magnetic systems at the Systems Integration and Test Facility (SITF) in Bldg. 970 and the other would be used to power the magnet system for experiments on Z. A schematic of

the systems planned for use at both facilities is shown in Figure 22. The diode and resistor system has been upgraded to be more efficient. The original system consisted of a single diode stack and 0.5Ω resistor in series with each module. The final system has a series/parallel combination of two diode-resistor legs. This design reduces the effective resistance in series with each module to 0.125Ω and improves the efficiency of the system by nearly 40%. As shall be discussed below, although this increased efficiency is not necessary for experiments at lower field, this improved efficiency may become important for achieving fields $\geq 30 \text{ T}$ on Z.

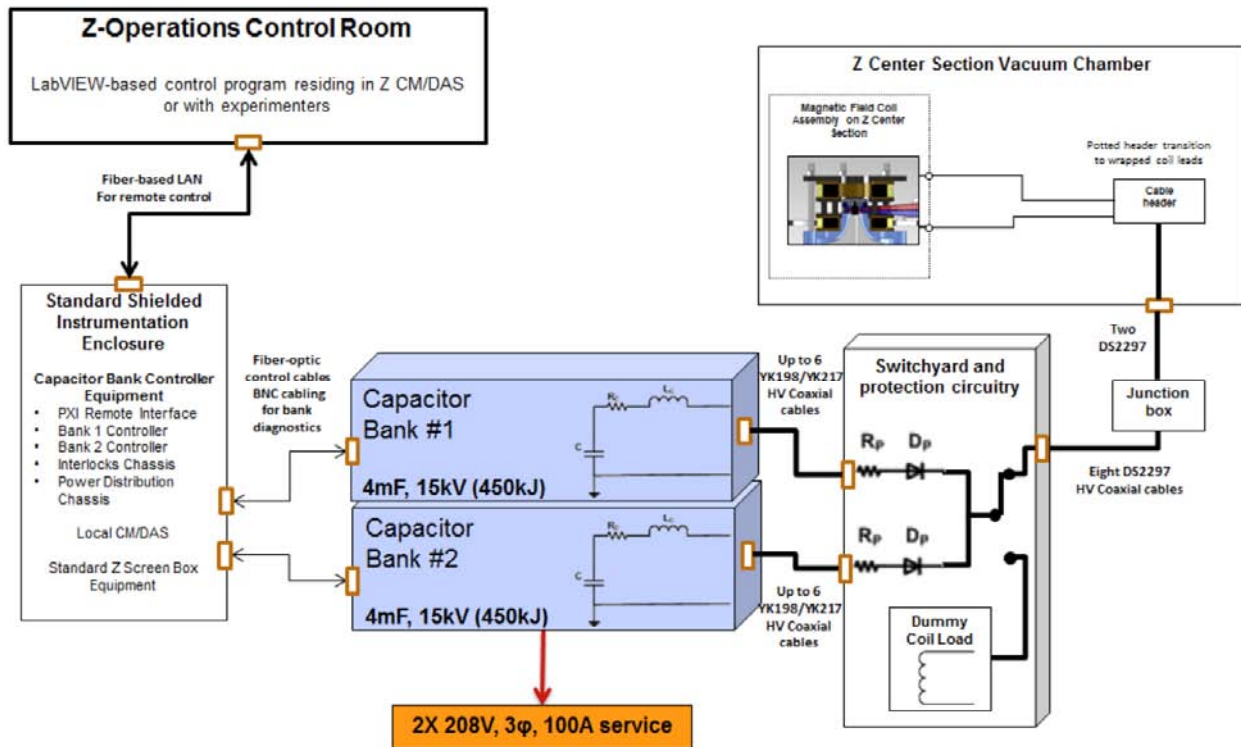


Figure 22: Schematic of the capacitor bank integrated into the Z facility.

The capacitance of the system is an important factor in determining the rise time of the pulse length due to the natural LC time constant of the system. The other parameter available is the inductance of the coil system. This is important to ensure that the system meets the pulse length requirement for proper target magnetization as described above and is also a factor in trying to reduce the forces on the load and feed hardware (longer pulses reduce the forces by reducing the induced voltages and currents).

3.3 Road map for coil design and development

It was realized during the conceptual design stages of the MagLIF coil system that the integration of the coil system with experiments on the proposed MagLIF experiments Z would not be trivial. This was primarily because of the priority placed on maximizing the achievable current on Z, which requires reducing the inductance of the power flow system (magnetically insulated transmission lines, convolutes and power feeds) to an absolute minimum. This basically translates to minimizing the length, height and volume of the system as much as

possible. Figure 23 shows how this reduces the space between the power feed and load to a bare minimum for a typical liner stability experiment.

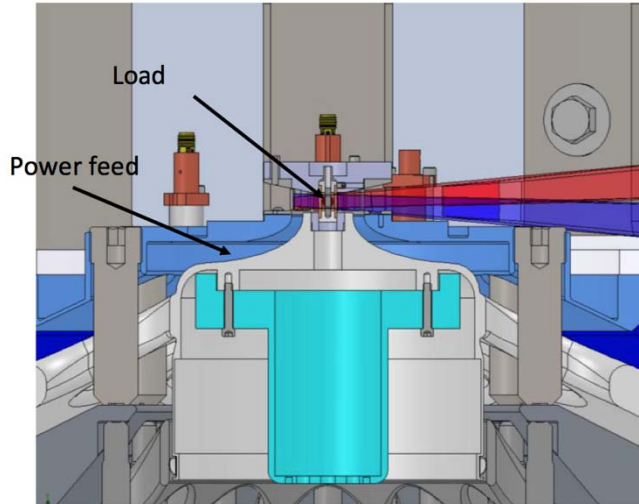


Figure 23: Standard low inductance power feed and load configuration. The example shown is from the "Lincoln 2" experiments in 2010.

The solution that became apparent was that we would need to extend the feeds vertically to accommodate the coil system while still keeping the inductance as low as possible. The question was how much extension was needed given all various constraints and requirements discussed above. One of the principles that guided the design was the desire to try and maintain one feed design (or at least the height) for each of the coil development stages anticipated for the MagLIF experimental program on Z. The three anticipated stages are shown in Figure 24. Figure 24a shows the full access option, which provides a large axial gap for full diagnostic access. Figure 24c depicts a possible final configuration where there is essentially no access for diagnostics. It is anticipated that this configuration would be of interest when the primary goal is to obtain and measure the neutron yield at the highest magnetic field achievable. Figure 24b shows an intermediate step where the gap is reduced to try and achieve intermediate field levels while still maintaining some radial access. This radial access could be used to provide radial diagnostic access (e.g. soft x-ray diagnostics) to probe the experiment during integrated MagLIF experiments where the magnetic field, preheat, and liner implosion elements are all combined. Alternatively, it could provide limited access to probe the liner radiographically for experiments studying liner stability in the presence of a magnetic field.

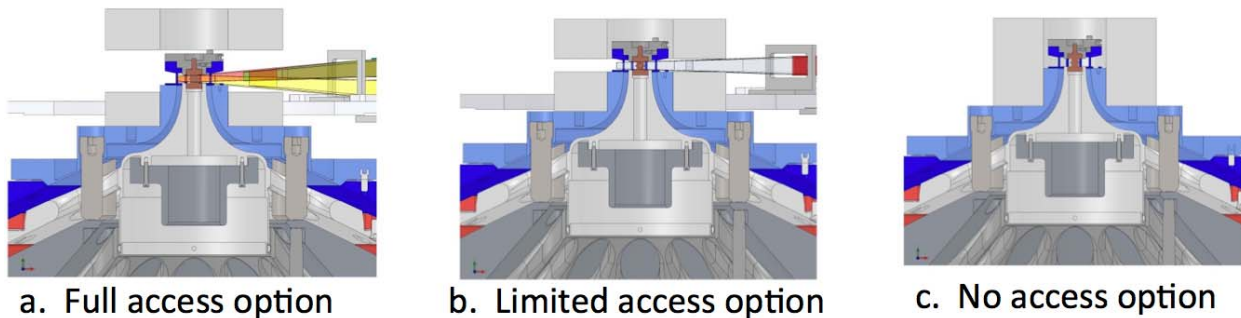


Figure 24: Notional road map for MagLIF magnet system integration and development.

Based on experience with state-of-the art coils designed and fabricated using internally reinforced construction techniques by the National High Magnetic Field Laboratory for the Sandia radiography program, one can get an idea of the height increase required. Table 2 lists the important coil parameters for two different magnets each with working bore lengths of 10 cm, i.e. peak field and mid-plane is at a height of ~ 5 cm. The first coil has a design field of 28 T with a working bore diameter of 110 mm (4.33 in.). The second coil has a design field of 50 T with a working bore diameter of 24 mm (.94 in.). Although these coils were designed to be operated cryogenically in a liquid nitrogen bath and designed with an intended lifetime of several hundred shots, their design and proven capability does provide some reassurance that ultimately achieving 30 T should be possible with a feed height increase of ~ 5 cm for our initial coil diameter of interest (~ 2 inches). This coil diameter was set by the desire for the coil system to fit around the outside of the standard slotted current return can.

Table 2: Key coil parameters for existing coil systems with coil lengths of 10 cm.

B Peak (T)	Inner radius (mm)	Outer radius (mm)	L (mH)	R @300 deg. K (mOhm)	I peak (kA)	E magnetic (kJ)
28	55	140	1.64	54.1	34.8	995
50	24	65	1.71	171	15.6	208

It should be noted that we have chosen to use a slotted stainless steel return-current can surrounding the MagLIF liner target as the baseline for the initial magnetized experiments on Z. This is because there are concerns that integration of the solid Be current return can used on some experiments could be problematic. The very thin-walled, high-aspect-ratio Be-can could easily buckle due to the induced magnetic radial pressure from the pulsed magnetic field. These considerations are only a concern when considering the need for diagnostic access. In the no access configuration shown in Figure 24c, it would be possible to use a solid stainless current return can. At such time it also would be possible to consider reducing the diameter of the system. The slotted current return can was originally sized to minimize the variations in B_θ due to current asymmetries for a slotted geometry. A solid annular canister would negate this issue. A smaller diameter would facilitate achieving higher applied B_z fields but impacts of increased feed inductance and possible increased current losses would need to be considered.

3.4 Demonstration of a 10 T, full diagnostic access MagLIF prototype

In CY2011 as part of a technical readiness demonstration effort, we designed, developed and tested a 10-T prototype of the full diagnostic access MagLIF prototype (Figure 24a). A prototype assembly of the split-magnet configuration required for the full-access configuration is shown in Figure 25. The coils shown in Figure 25 are unfinished fabrication prototypes and were used in this picture to emphasize both the location of the coils and the traditional wire wound solenoid construction that we used. The cross section of the finished prototype coil shown in Figure 26 illustrates how the monolithic build of magnet wire is lined with an outer band of azimuthally wound Zylon. Zylon is a high strength epoxy fiber composite that is used to support the large radial forces acting on the wires.

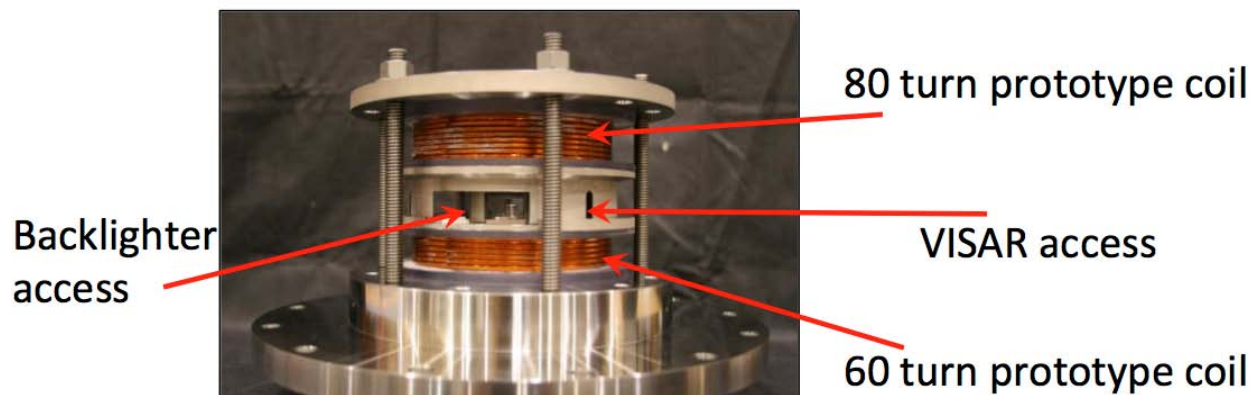


Figure 25: A 10-Tesla MagLIF prototype assembly with test windings of coils.

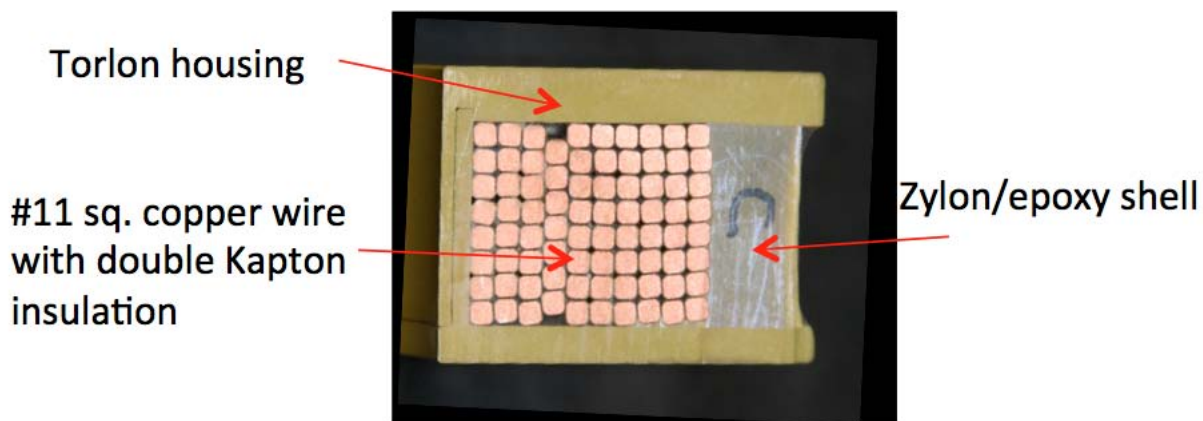


Figure 26: Cross-section of un-shot 80-turn top coil.

A key design consideration for these coils was the peak stress in the Zylon composite. Based on past experience and data from literature on the strength of Zylon composites, a peak stress of 2 GPa was used to estimate the design field strength for the magnet system. Based on this design parameter, analytical stress calculations in the Zylon fiber using radial Lorentz forces output from our magnetic field solvers suggested the design field strength for these coils was about 13 Tesla. This gave us some confidence that reliable operation at 10 T was feasible. Unfortunately, results from some preliminary testing of three prototype coil systems reminded us that the realities of pulsed coil systems are complex and are not always easily captured in a single design parameter. Late last year, in an initial effort to characterize the lifetime and reliability of our design, we built and tested three prototype coil systems in the Magnetic Coil Test Bed (MCTB) in SITF (Figure 27a). The first coil pair operated successfully for 17 pulses (Figure 27b) and then experienced a layer-to-layer “soft” electrical failure after peak field during the 18th pulse. Coil pairs #2 and #3 had some issues during fabrication that may have affected their performance. Coil pair #2 experienced a similar failure during its second pulse at 10 Tesla. Because of these issues and early failure, we chose to test the reliability of coil pair #3 at a reduced field of 7 T. Coil pair #3 has successfully operated for more than 10 pulses at 7 T with no signs of cracking or mechanical distortion.

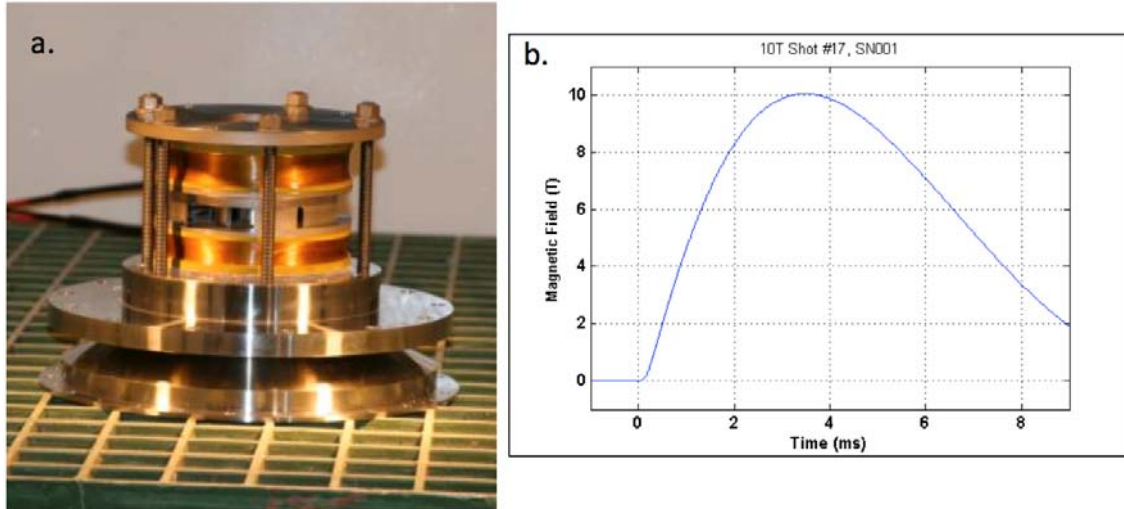


Figure 27: (a) A 10-T MagLIF prototype shown inside the SITF test chamber. (b) The measured field pulse recorded during an SITF experiment with this prototype.

Based on these experiences, we are working to reinvigorate our coil engineering efforts. The full-access system with its split construction is particularly challenging. The cause of coil failures can be subtle and difficult to diagnose. Figure 28 shows the post-mortem cross sections for Coil set #1. As expected, there is some permanent radial deformation of the magnet wire at the inner radius. Some epoxy potting voids and gaps are also visible. The Zylon shell appears to be intact. We are unable to determine the location and cause of the soft electrical failure from this post-mortem. We speculate that voids in the layer-to-layer transition may have allowed movement of the wires, which subsequently led to failure of the electrical insulation. We are working to improve our fabrication techniques and eliminate the epoxy voids and to develop repeatable, reliable construction techniques. In the longer term, it is believed that we need to perform more detailed analysis of the coils. Coil systems can tolerate strains of 1 – 2% with lifetimes decreasing as strain increases. Performing detailed finite element stress analysis will help us better benchmark our designs against this strain metric. It will also guide our coil development and help us to decide when it will be necessary to implement more state-of-the-art design and fabrication technologies including stronger wire (e.g. Glidcop) and internal reinforcement (intermediate layers of Zylon between wire layers that limit the strain in the system).

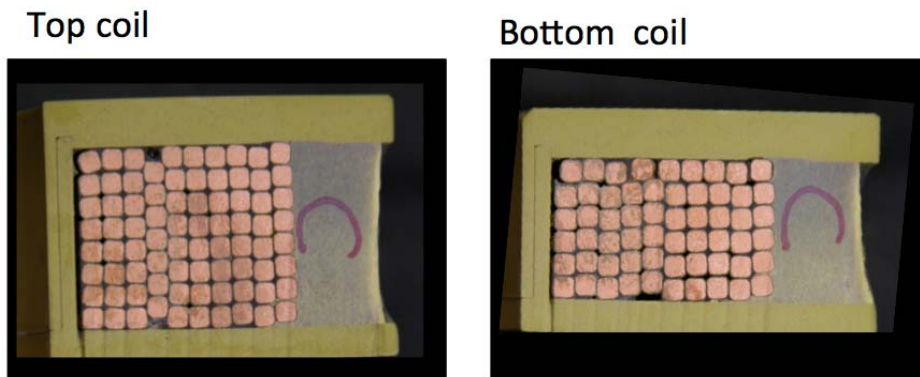


Figure 28: Post-mortem cross-sections of prototype coil set #1 after a soft failure during its 18th pulse at 10 T. No obvious indicator of failure is visible.

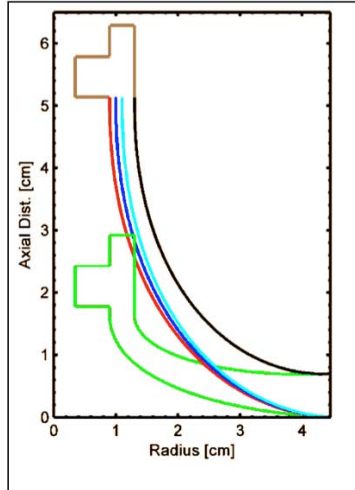
The requirement on the length of the magnetic field rise time is determined by the need to allow the field to penetrate through the liner without deforming or crushing the target [Ref: Slutz et al, Phys. Plasmas, 17, 056303 (2010)]. Following the techniques described there, the calculated safety factors for yield and buckling [Ref: Rovang et al., MagLIF Workshop 2012, SAND2012-0884C] are presented in Table 3 for the 10-T prototype (which has a rise time of 3.49 ms) for two liner materials of interest, Be and Al 1100. The projected safety factors for a second 30-T system with an estimated rise time of 6.65 ms are also listed. It should be noted that the yield safety factors are independent of the liner aspect ratio while the buckling factors listed are for a liner aspect ratio of 10 (radius / thickness). Lower aspect ratio or thicker liners will be more resistant to buckling. It appears that there is plenty of safety margin at 10 T for either material and also for Be at 30 T, however, buckling of Al 1100 targets at 30-T may be an issue. We plan to test real targets in SITF before conducting experiments on Z.

Table 3: Engineering safety factors for MagLIF targets.

Material	Field (T)	Rise time (ms)	Yield Safety Factor	Buckling Safety Factor
Be	10	3.49	82.7	89.7
Al 1100	10	3.49	37.4	13.9
Be	30	6.65	17.5	19.0
Al 1100	30	6.65	7.9	2.9

3.5 Z experiments studying power flow in coil-compatible hardware

A series of Z experiments in March 2012 (named “Washington-1” on the Z shot schedule) were conducted to test the extended power feeds required for magnetic field coils (e.g., see Figure 24). The experiments tested three different feed gap dimensions as illustrated in Figure 29. The current at the entrance to the power feed were measured using load B-dots, and the current at the load was measured VISAR probes located in a cavity above the liner, after the power feed gap. The current return can in these experiments was a solid beryllium return can, which permitted the liner target to be radiographed. Figure 30 shows experimental results for the load current B-dots and VISAR respectively. As anticipated, the increased inductances resulted in significant current reduction. The B-dot measurements in Figure 30a are reduced relative to the standard low-inductance hardware configuration, which suggests that the current losses occurred outside of the extended power feed, in the post-hole convolute region. The lowest losses and highest currents were obtained with the 2-mm gap. The velocity trends shown in Figure 30b appear to be consistent with the load-Bdot trends in that the highest velocities (and thus highest load currents) were achieved with the smallest output gaps (lowest inductances). However, the smallest output gap tested (i.e., 2 mm) seemed to result in more azimuthal asymmetry in the power delivery, in that the probes showed more variation from one azimuthal position to another.



MagLIF inductance

Feed 1: 5.52 nH (7 mm to 4 mm)

Feed 2: 4.82 nH (7 mm to 3 mm)

Feed 3: 4.18 nH (7 mm to 2 mm)

Standard feed inductance:

Feed = 3.97 nH (7 mm to 4 mm)

Figure 29: Plot illustrating the dimensions of the three extended power feed geometries used in March 2012 "Washington-1" experiments on Z, compared with the standard power feed dimension used in most liner stability experiments.

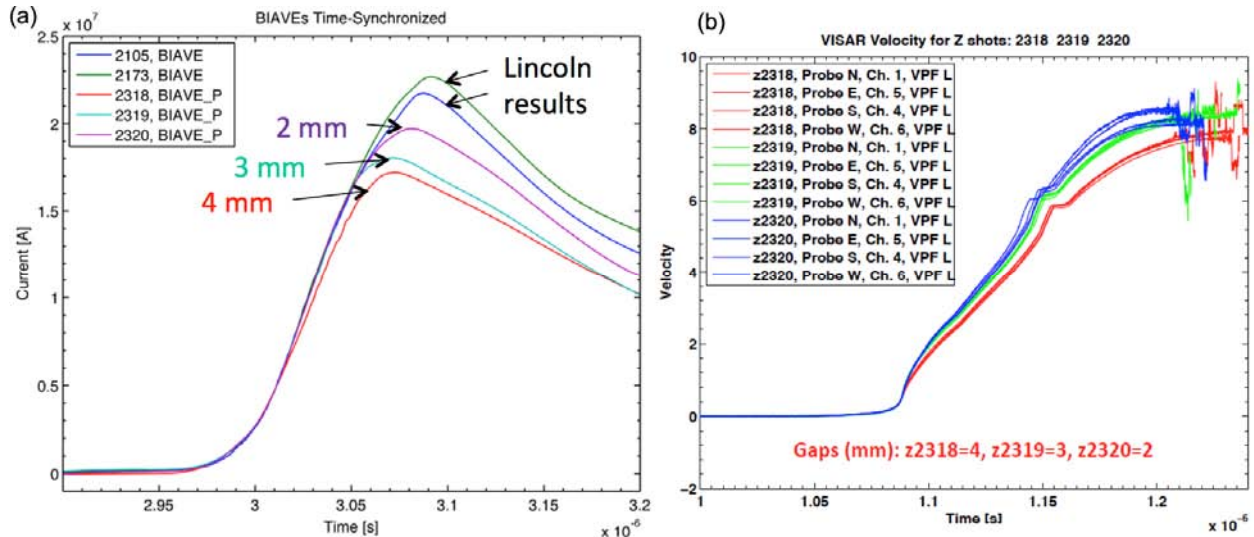


Figure 30: (a) Plots of the upstream load B-dot current measured during Washington 1 experiments using an extended power feed, compared to a baseline experiment ("Lincoln") using a standard feed configuration. (b) Preliminary VISAR probe velocity unfolds for the Washington-1 experiments.

These results show the trade-off between limiting the vertical extent of the power feed in order to maximize the drive current and providing more room for achieving higher magnetic fields. A possible alternative that might reduce the losses associated with higher feed inductances and provide more radial room for the magnets is to combine MagLIF with a 31-cm convolute, which is much larger than the standard convolute. A notional representation of this concept is shown in Figure 31. The "Chaves" experiment conducted in October 2011, which used a 31-cm convolute, delivered the same current to the load as a standard convolute and power feed despite an additional 1.8 nH inductance in that hardware. This suggests that it might be possible to field even the most inductive power feed tested in Washington, i.e., the 4 mm gap with an additional 1.55 nH of feed inductance, without any noticeable loss in current.

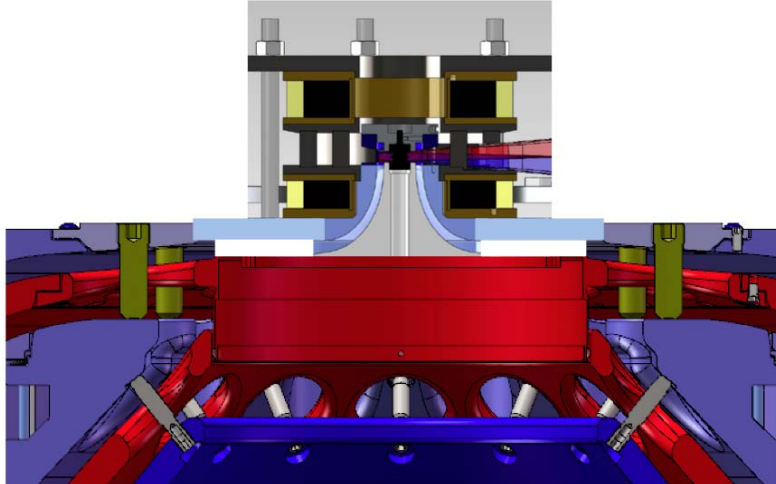


Figure 31: Conceptual design of MagLIF magnet system on a 31-cm convolute.

3.6 Design status of experimental hardware for the first magnetized preheat and magnetized Z experiments in 2013

The 10-T prototype hardware shown in Figure 25 only considered the need to provide full access for VISAR and the 2-frame backlighter. Recently, additional requirements were identified to support diagnostic access for combined magnet and preheat experiments planned for next year. Figure 32 shows a map of all the requested diagnostic access presently being considered for the full-access configuration. The lines-of-sight are mapped to the existing two-ring support structure made from a titanium alloy (Ti-6Al-V4) that support the large attractive magnetic between the force (nominally 33, 000 lbf) between the top and bottom coil. We are now reviewing the design of the support structure to accommodate these diagnostics. It may be that a single ring system would be better suited to meet the full diagnostic requirement.

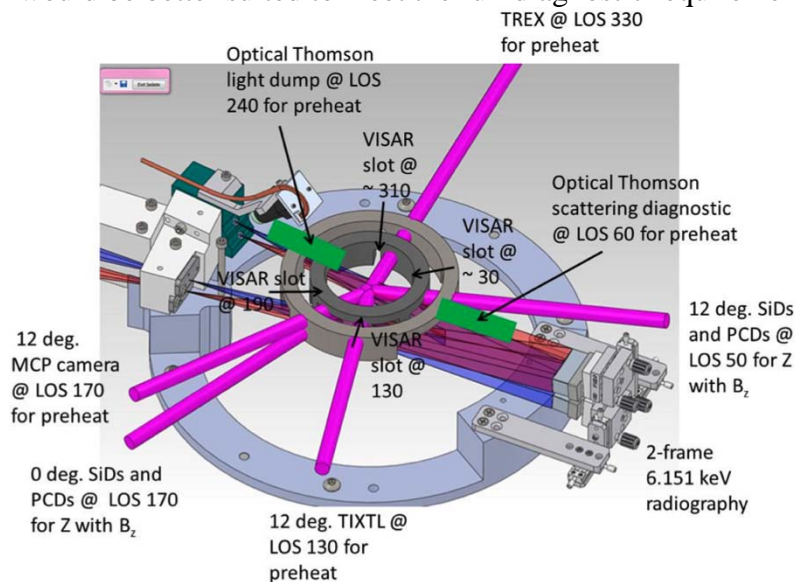


Figure 32: Schematic diagram of the design layout for all the diagnostics requested for magnetized preheating and Z experiments in 2013. The experiments will use the full-access configuration for the magnetic field coils.

Figure 33 shows the design of the load hardware planned for the initial magnetized experiments on Z with the existing two-ring support structure. We recently became concerned about the stress on the breakaway grooves in this hardware due to induced electromagnetic forces from the magnetic field coils. Previous analysis had suggested that these forces might be sufficient (thousands of Newtons) to be of concern. We ran detailed calculations of the transient electromagnetic forces and generated estimates for the force amplitude on the hardware (Figure 34). These were input to a detailed static mechanical Finite Element Analysis calculation. Figure 35 illustrates that at 10 T there may be some very slight localized yielding in the breakaway groove closest to the load. We plan to confirm these results with testing in SITF over the coming months. These results reinforce the need for detailed engineering and analysis of these complex systems. It also indicates that a redesign of the breakaway grooves may need to be considered at higher fields as we go forward.

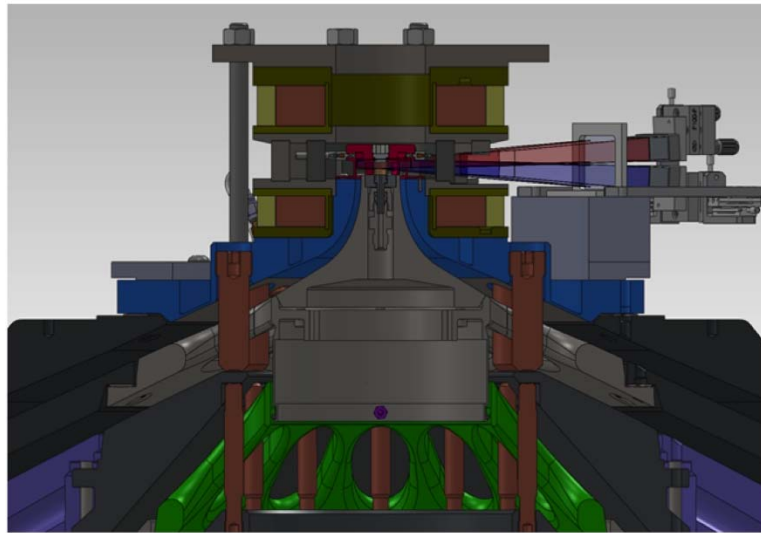


Figure 33: Design layout showing final feed designs for the first magnetized experiments in 2013.

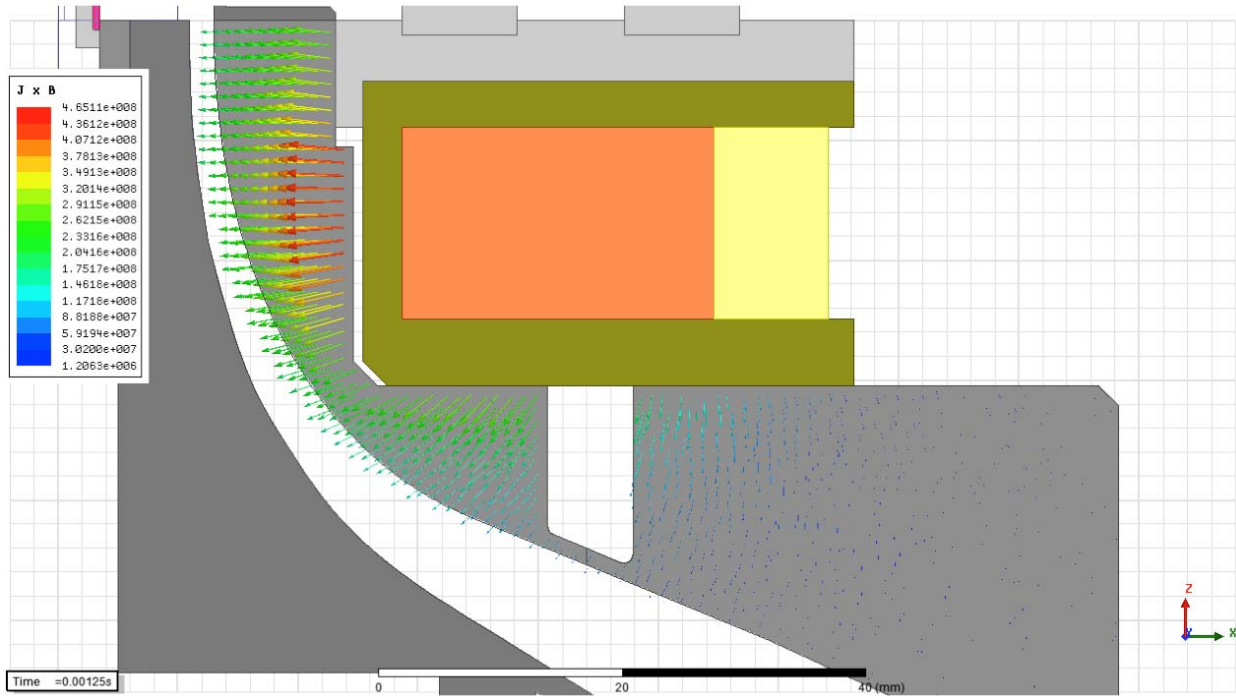


Figure 34: JxB force distribution on the upper anode from transient electromagnetic analysis (t=1.25 ms).

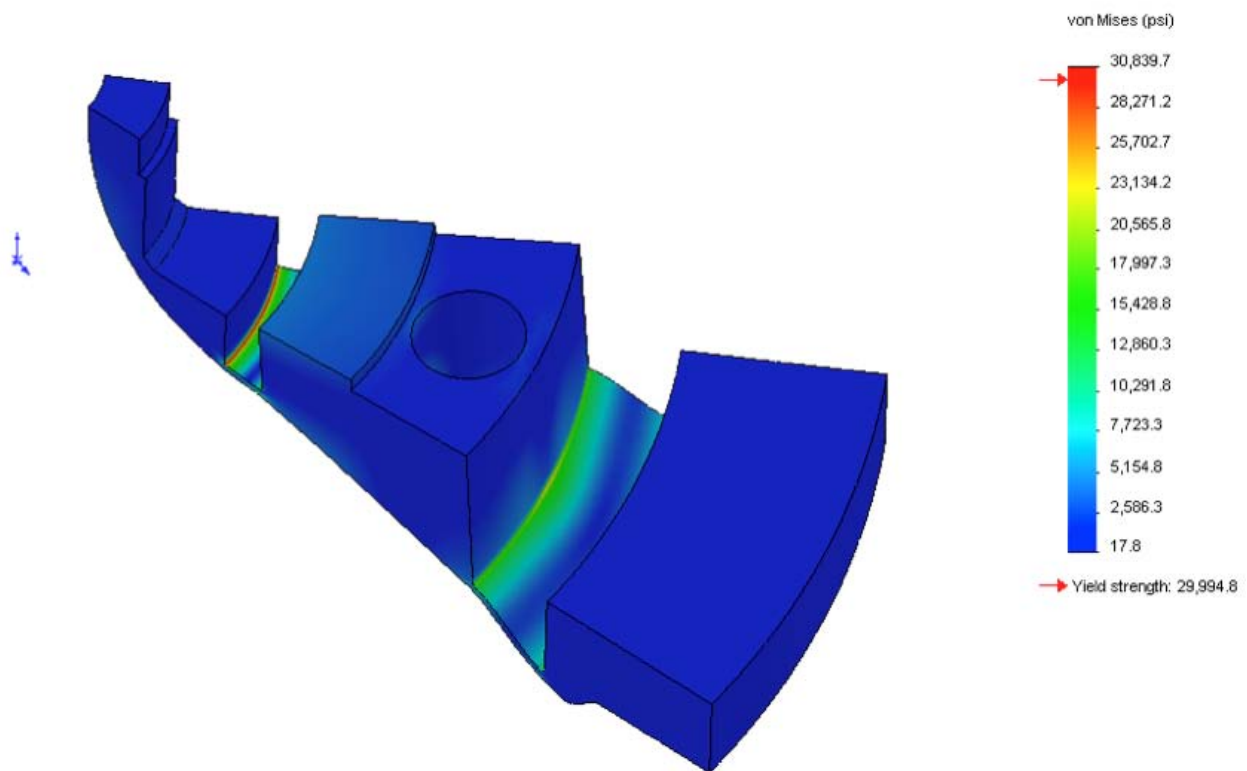


Figure 35: Calculated von Mises stresses from static mechanical finite element analysis of the upper anode. The stresses shown are from a 10-T magnetic field.

4. MODELING OF MAGNETIZED LINER FUSION CONCEPT

4.1 Introduction

The original simulations of the Magnetized Liner Inertial Fusion (MagLIF) concept described in Section 1 and published as part of this LDRD [3] were done using the LASNEX code. LASNEX has been one of the primary inertial confinement fusion simulation tools for decades. It has numerous capabilities developed to support designs for radiation-driven spherical capsule implosions on the National Ignition Facility. Since that facility relies on intense laser beams to heat and create matter, it has the capability to simulate not only the magneto-hydrodynamics (MHD) of the liner implosion and the embedded magnetic field, but also the laser preheating. Since the users of the MHD packages in this code are relatively few in number and little data exists to benchmark these calculations, however, there remain questions about the validity of its predictions in many areas.

Our first area of concern was the validity of the calculations for the magneto-Rayleigh-Taylor (MRT) instability, which led to the proposal for this LDRD project. This was a major area of concern because the results of MagLIF calculations were very sensitive to the choices made in setting up the simulations and the resulting degree of the MRT growth. As described in Section 2 of this report, however, LASNEX appears to be capable of doing a reasonable job with MRT growth calculations. The main limitation seems to be that LASNEX is limited to two-dimensional calculations, and the data clearly shows at least some degree of three-dimensional structure.

A second area of concern is the ability of LASNEX to calculate the effect of higher-order MHD terms such as the Nernst term. This term affects the ability of the liner to trap the magnetic flux during the compression, and to our knowledge this effect has never been experimentally tested and the results used to validate the simulations. We did not attempt to address this effect in this LDRD, because it requires magnetized, preheated fuel inside of a convergent target to test. Essentially, the integrated MagLIF experiments will ultimately be the test of the validity of these calculations.

A third area of concern is the ability of LASNEX to calculate the amount of preheating by the laser of the fusion fuel. Given that LASNEX has been used for many years to calculate the radiation from hohlraum walls and other targets heated by lasers, and validated against this data, we are not greatly concerned that the calculations will be wrong here. On the other hand, there may be subtle focusing effects of the laser light in the fuel that we are not properly taking account of. Moreover, the gradients in the heated fuel can create spontaneous grad-n X grad-T magnetic fields that in some cases are estimated to approach a Tesla [23]. Such laser-induced magnetic fields may complicate the field line structure of the seeded axial magnetic field in detrimental ways.

There are other issues with our LASNEX calculations of the MagLIF concept, such as anomalous diffusion of particles across field lines, but we have attempted to assess the impact of such issues computationally and feel that the above three issues remain our most important concerns at this time [3].

A more pressing issue for the Sandia ICF program is that LASNEX may eventually be phased out in favor of a new ICF code named HYDRA. HYDRA is an arbitrary Lagrangian-Eulerian 3D ICF code that can be run in parallel on many processors, both features of which are clearly advantageous. The HYDRA code includes the following packages for modeling physical processes relevant to the MagLIF problem: 3D laser light raytracing, 3D resistive MHD and a circuit model, multi-group diffusion approximation or monte carlo thermonuclear burn, multi-group diffusion approximation or implicit monte carlo radiation, local thermodynamic equilibrium (LTE) and non-LTE opacities and equations of state, QLMD conductivity tables, and multi-block meshing capabilities. HYDRA is playing a key role in the ongoing National Ignition Campaign and has been well validated. Its main disadvantage relative to LASNEX was that the MHD package was relatively new at the start of this LDRD project and required substantial verification and validation on MagLIF-related problems. The same major issues noted above for LASNEX also apply to HYDRA calculations.

To summarize, a key portion of this LDRD effort was aimed at improving our modeling capabilities using both LASNEX and HYDRA. Most of our detailed comparisons to the liner stability data in Section 2 were done using LASNEX, since we already had a large body of published calculations made using this code and were keenly interested in understanding their validity. In parallel, we were pursuing the development of HYDRA by using it for integrated MagLIF calculations and preheated fuel calculations. A number of substantial improvements to HYDRA were a direct result of the MagLIF modeling effort supported by this LDRD.

4.2 High-yield, high-gain magnetized liner targets

The MagLIF concept has the potential to substantially ease the difficulty of reaching the extreme plasma conditions required for significant fusion yields. For example, instead of the ~ 300 - 400 Gbar pressures required for ignition and ~ 1 MJ yield in a NIF capsule, MagLIF has the potential to produce substantial yields (~ 100 kJ) on Z at pressures of ~ 5 Gbar. However, it was widely accepted that magnetized inertial fusion had little potential for achieving high gains, because magnetic fields tend to inhibit the propagation of a burn wave into the surrounding layer of cold, dense DT fuel. High-gain targets would greatly help in achieving the high yields needed for NNSA missions and gains >10 are a requirement for any future fusion power plant. Thus, after this project completed the initial study and documentation of the MagLIF concept [3], it began to examine this important question.

The results of our analysis of this question have already been published in Physical Review Letters in 2012 [13], so we summarize them only briefly here. A series of one-dimensional and two-dimensional LASNEX calculations were done of the configuration shown in Figure 36. The primary modification to the standard MagLIF design is the addition of a dense cryogenic layer of DT fuel on the inside surface of the metal liner. The operation is otherwise essentially the same as the original MagLIF concept. Exterior field coils (not shown) provide an initial axial magnetic field of 10-30 T. A laser beam enters from above to preheat the central portion of the fuel before the liner implodes. The liner is imploded by the large azimuthal magnetic field induced by the drive current from a pulsed power accelerator such as Z. During the implosion a hot spot is formed from the preheated fuel, which is compressively heated above the ignition temperature

with modest liner convergence ratios of 15-25, where the convergence ratio is defined as the ratio of the initial over final radius of the inner surface of the liner.

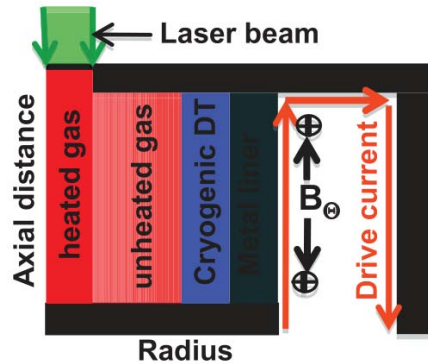


Figure 36: Schematic diagram of a high-gain, high-yield MagLIF target.

The simulation study indicates that the required hot spot areal density for propagating burn is very weakly dependent on the hot-spot density in the range $0.1\text{-}10\text{ g/cm}^3$. It does, however, depend significantly on the areal density of the liner. This is because the liner areal density determines the inertial confinement time. A longer confinement time allows burn wave propagation with larger magnetic inhibition of the transport, thus allowing hot-spot ignition at lower areal densities, e.g., a hot-spot areal density of 0.03 g/cm^2 is sufficient for propagation with a liner areal density of 10 g/cm^2 .

Two-dimensional LASNEX scaling calculations of the configuration in Figure 36 were done using a circuit model. The circuit source voltage was varied to obtain peak currents ranging from 30-70 MA, rising to peak in about 100 ns. The initial DT gas density ($5\text{-}10\text{ mg/cm}^3$), ice layer thickness, magnetic field strength (10-30 T), laser pulse length (10-30 ns), and timing were optimized for each value of the peak current. These simulations indicate hot-spot densities of $5\text{-}10\text{ g/cm}^3$, peak cold fuel densities of $100\text{-}250\text{ g/cm}^3$, and radial burn wave propagation into the cold fuel producing large yields as shown in Figure 37. The gain for a standard MagLIF design is about 8 at a peak driving current of 60 MA, while the high-gain MagLIF simulations using a cryogenic layer has a gain exceeding 100. The improvement over the standard MagLIF concept becomes very pronounced at currents above 55 MA, and the simulated gain of the high-gain MagLIF target exceeds 1000 at a peak current of 70 MA. Over the range of peak currents from 30 to 70 MA, the optimum magnetic field decreases monotonically from 30 to 11 T, and the optimum laser energy increases monotonically from 8 to 22 kJ.

More details of these designs, including their sensitivity to various settings and assumptions in LASNEX, are documented in the publication on this work [13].

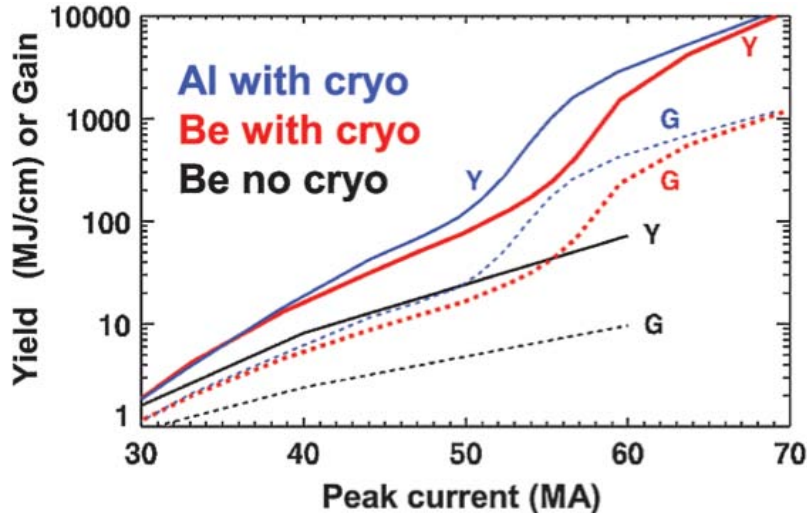


Figure 37: Simulated yields (solid curves) and gains (dashed curves) plotted as a function of peak drive current. The black curves are for standard MagLIF while the colored curves are the results for MagLIF simulations that include a cryogenic layer of DT ice on the inner surface of a liner (beryllium shown as red, aluminum as blue).

4.3 Integrated MagLIF calculations using HYDRA

As noted in Section 4.1, a significant effort to develop integrated MagLIF calculations using HYDRA was a part of this LDRD project. A series of calculations in one, two, and three dimensions were conducted to model the MagLIF targets and to determine how well HYDRA could model the relevant physical processes.

As a first step, the preliminary 1D point design for the MagLIF concept was modeled in HYDRA. The beryllium liner had an aspect ratio of 6, initial inner radius of 2.6 mm, and total mass of 180 mg/cm. Within the liner, the DT gas had an initial density of 3 mg/cc and applied Bz magnetic field of 30 T. The liner was imploded with peak possible ZR parameters (a charge voltage of 95 kV and a peak current of ~ 27 MA). During the implosion, ~8 kJ of laser energy was uniformly deposited within the DT fuel (without the laser deposition package in HYDRA) to an ion temperature of about 250 eV. The liner reached a peak implosion velocity of approximately 83 km/s, well below typical ICF implosions. The total fuel absorbed energy was 113 kJ/cm, while the whole target (fuel plus liner) absorbed 1026 kJ/cm. At stagnation, the convergence ratio was 22, the stagnation pressure was about 5 Gbar, the Bz magnetic field reached 80-220 MG, the ion temperature reached 6-8 keV, the density was ~1 g/cc, and the fuel and liner R values were ~0.01 and ~1 g cm⁻², respectively. The time of peak burn coincides with the time of stagnation, and achieved peak energy and neutron production rates of 383 kJ/cm/ns and 1.36e17 neutrons/cm/ns, respectively. The 10%-90% burn duration was approximately 4-5 ns. By the time the target disassembled, the total fusion output was 1130 kJ/cm with a neutron yield of 4e17 neutrons/cm, representing a gain of 10 relative to the fuel and 1.1 relative to the entire target.

Integrated MagLIF experiments will include numerous multi-dimensional and non-ideal effects, which ideally should be captured in an integrated model of the experiment. The additional

parameters and design constraints of the laser, the laser entrance hole (LEH) and its gas-containing window, the liner, the Z generator (circuit model), the electrode end caps, and the relative timing of the implosion and preheating must be self-consistently included in a single simulation in order to optimize the system. These calculations used a very complex, 2D or 3D multi-block mesh in order to include all of the relevant details for an integrated MagLIF experiment, shown in Figure 38. For instance, unlike single block meshes, multiple enhanced and reduced points of connectivity between blocks allow for fine zoning on all relevant surfaces and corners, but only where desired (and not elsewhere); this allows us to simultaneously well-resolve the physics of the laser entrance hole at the top of the target and its window, all anode and cathode surfaces, the inner and outer boundaries of the liner, and also non-rectangular surfaces, if desired. These mesh types allow us to investigate problems at a level that would be intractable for a single-block, single-processor code.

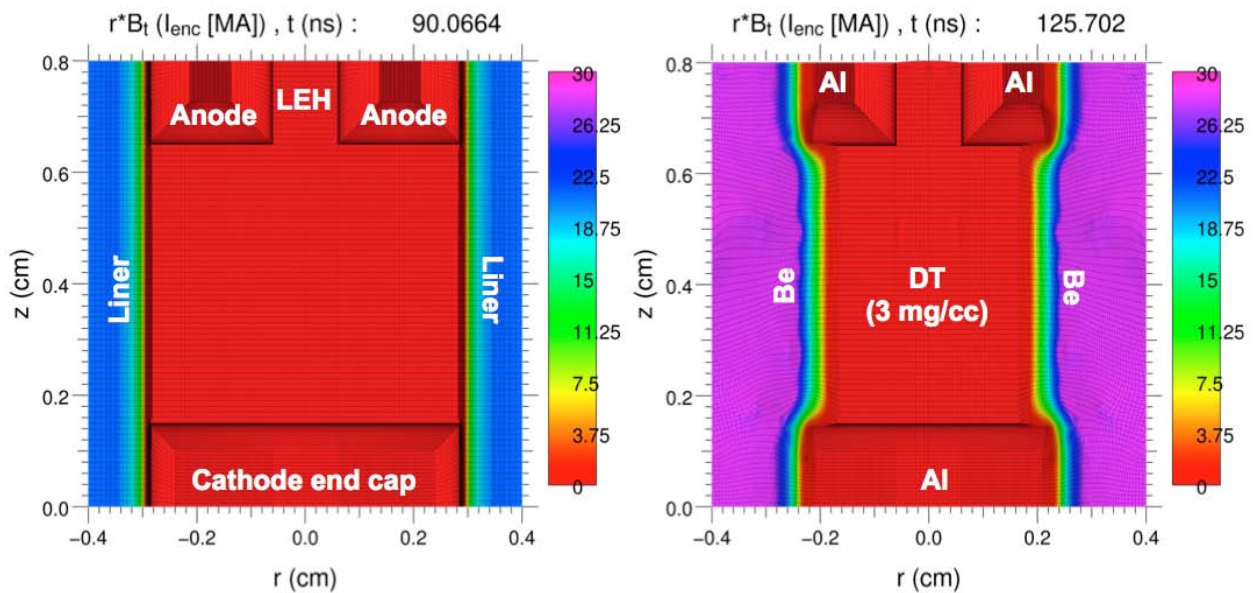


Figure 38: An example of the complex, multi-block mesh that is required in HYDRA in order to capture all of the relevant integrated details. This meshing allows for fine ablation zoning on all surfaces (where it is needed).

Regarding the laser parameters, the simulation input is the energy, spot size, pulse duration, and focal plane location. Asymmetric one-sided preheating necessitates evolving $T(r,z,t)$ and $B(r,z,t)$ while heating the gas to the required ion temperature (T_i), which itself is specific to the other integrated implosion parameters. Also, the preheat laser must not ablate significant anode material, due either to small amounts of energy in its extremities or beam pointing error, to the point that it closes the LEH before the end of the heating phase. To self-consistently model the shock generated by the laser striking the LEH window and laser refraction due to expanding window material, the LEH material, thickness, and location must be included in the integrated model. The window must hold the gas pressure (<25 atm) but not absorb too much of the laser energy ($\rho_{win}\Delta z_{win} \ll \rho_{gas}\Delta z_{gas}$), and also be recessed relative to the main fuel region so the heated plasma pressure prevents window material from mixing with the fuel underneath the liner. The presence of the electrode end caps provide material boundaries for the LEH and burn region, and need to be included in an integrated model. The LEH needs to be large enough to allow sufficient laser deposition while keeping the laser irradiance from becoming too high, but also

small enough to reduce hydrodynamic flow losses of preheated gas out the LEH during the implosion phase. The presence of the end cap walls introduces a number of wall effects, as well, such as liner-wall instability, loss of fuel energy to the wall and LEH, the fact that the B_z field is “frozen-in” to the highly conductive non-imploding adjacent walls, and laser and radiation ablation wall effects (if not designed around). Laser deposition parameters and timing are specific to the implosion, and avoidance or mitigation strategies are needed to prevent laser ablation of the high-Z cathode material into the fuel underneath the liner. For example, if the laser directly irradiates the far cathode wall material, it will ablate material that can very rapidly (>2 mm/ns) move into the gas beneath the liner (before the liner fully implodes) and mix with the fuel, spoiling the implosion. Another concern during the preheating process is that the laser-heated plasma has high beta (plasma pressure to magnetic field pressure), and so can readily advect the magnetic flux. Inhomogeneities in the magnetic field profile, gas density and temperature, and liner density due to MRT must all be evaluated simultaneously, since the evolution of each affects the others. Eventual integrated high-resolution simulations in 3D offer the possibility of the most realism in terms of modeling magneto-Rayleigh Taylor (MRT) instability and its effect on the stagnation plasma, when all the aforementioned effects are included. Most critically, the liner and circuit parameters (such as material, mass, aspect ratio, length, surface roughness, fuel density, and B_z0 strength, charging voltage, and load inductance) need to be matched to achieve the requisite velocity, B_z^{stag}/B_z0 , convergence ratio, stability, ion temperature, and R needed to achieve conditions that produce plentiful yield. In summary, the optimal combination of considerations for integrated simulations may not be identical, or even very similar, to those for idealized simulations.

Progress has been promising and ongoing in 2D and 3D integrated MagLIF simulations using HYDRA, and code development occurs in tandem with these studies. Some example integrated 2D simulations of a MagLIF target are shown in Figure 39. Recently we have succeeded in running these calculations all the way through to stagnation, as shown in Figure 40. This is a significant step forward, as early attempts in the LDRD at doing so ran into problems with various code packages in HYDRA. A number of substantial improvements to HYDRA were a direct result of the MagLIF modeling effort, and associated coordination with the HYDRA developers, conducted under this LDRD. New boundary conditions now allow both a driving B_θ magnetic field component in addition to a prescribed background B_z magnetic field component. The code now models anisotropic conductivity in the presence of a B_z magnetic field. Charged particle transport, such as required for the fusion product alpha particles, now accounts for the presence of a B_z magnetic field. Further improvements are underway, such as the inclusion of thermoelectric effects due to Nernst and Righi-Leduc (thermal Hall) terms in the MHD package, and will be followed by careful testing in coordination with HYDRA developers.

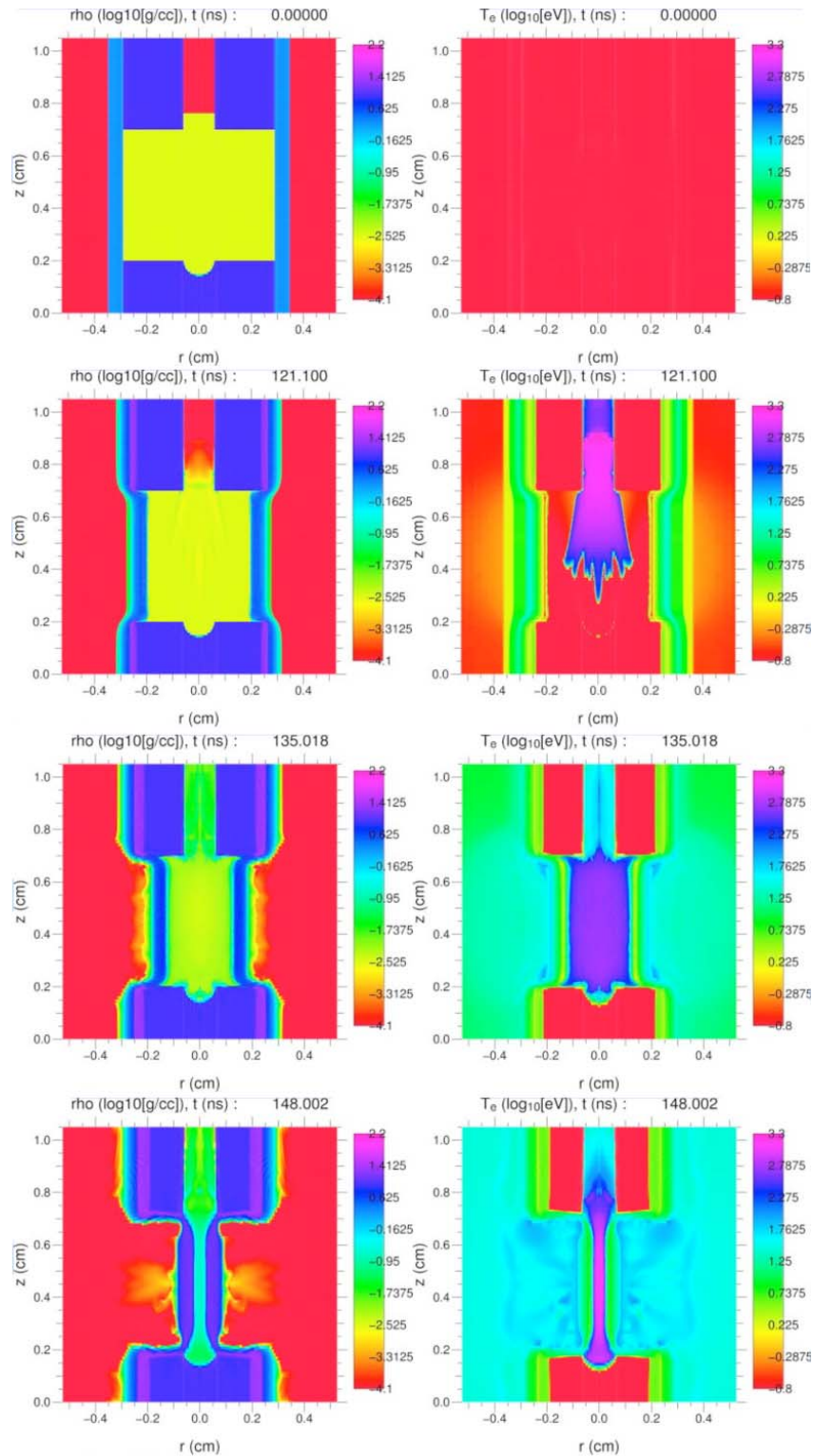


Figure 39: Example HYDRA simulation results from four selected times. The left plots indicate the density and the right plots the electron temperature, both on a log scale. The examples show the state (a) just prior to the start of current, (b) midway through the laser preheat pulse, (c) shortly after the preheated fuel has equilibrated, and (d) a few ns prior to stagnation.

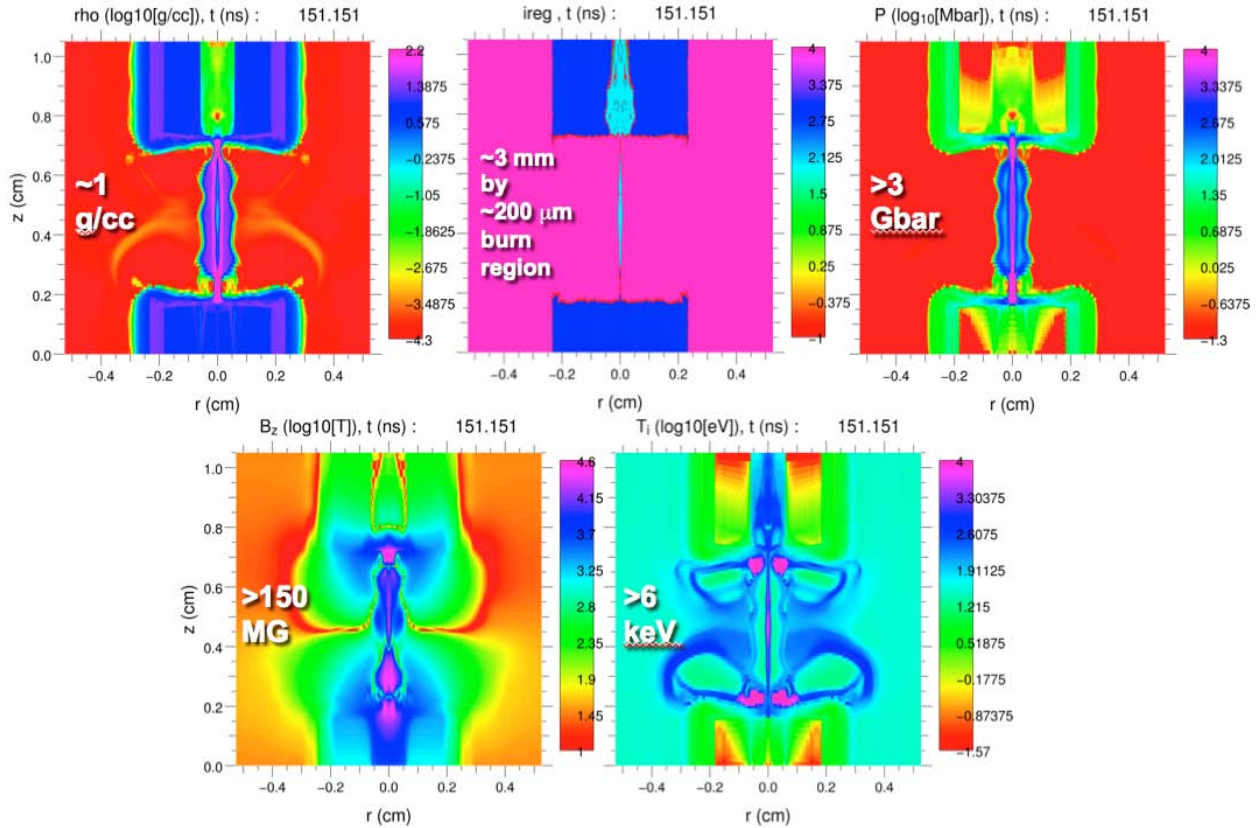


Figure 40: Example HYDRA plots indicating the final conditions achieved by a MagLIF target. The simulations shown are fully-integrated HYDRA calculations.

In summary, HYDRA has been significantly improved to be able to run problems of interest for MagLIF. Design work is underway for the first integrated experiments planned in 2013. The first experiments will use the existing available capabilities on Z and Z-Beamlet (~ 2.5 kJ of laser energy, D₂ gas, $B_z=10$ T, and 85 kV charge voltage on Z). The code will be benchmarked against standalone preheat experiments, liner and B_z flux compression experiments, and these first integrated experiments. This will enable us to develop an integrated design in the following years that may achieve scientific break-even fusion yields as the available capabilities are improved (~ 6 - 8 kJ of laser energy, DT gas, $B_z=30$ T, and 95 kV charge voltage on Z). The long-term goal is to use the data from Z to benchmark integrated calculations to predict the performance of these targets on future facilities. For example, we would like to assess high-gain MagLIF targets with a cryogenic DT ice layer design (as discussed in Section 4.2) in integrated HYDRA simulations.

5. INVITED PRESENTATIONS, PUBLICATIONS, AND AWARDS SUPPORTED BY THIS PROJECT

5.1 Invited presentations

This LDRD project made significant contributions to a number of invited talks at conferences across the world. Below we list invited talks that were largely supported by LDRD funding. In addition to the talks listed below, there were a large number of contributed papers submitted to these and other conferences.

“Magnetized Liner Inertial Fusion,” invited talk presented by Stephen Slutz at the American Physical Society Division of Plasma Physics (APS-DPP) meeting in Atlanta, GA, Nov. 2-6, 2009.

“Measurements of Magneto-Rayleigh-Taylor Instability Growth in Solid Liners on the 20 MA Z Facility,” invited talk presented by Daniel Sinars at the International Conference on Plasma Science (ICOPS) meeting in Norfolk, VA, June 21-24, 2010.

“Measurements of Magneto-Rayleigh-Taylor instability growth in initially solid liners on the Z facility,” invited talk presented by Daniel Sinars at the American Physical Society Division of Plasma Physics (APS-DPP) meeting in Chicago, IL, Nov. 8-12, 2010.

“Beryllium liner z-pinch implosions for inertial confinement fusion and dynamic materials studies at the Z pulsed-power facility,” presented by Ryan McBride at the 3rd International Conference on High Energy Density Physics in Lisbon, Portugal, May 17-20, 2011.

“Measurements of Magneto-Rayleigh-Taylor instability growth in initially solid liners on the Z facility,” presented by Daniel Sinars at the Dense Z-Pinch (DZP) meeting in Biarritz, France, June 6-9, 2011.

“High-gain Magnetized Liner Inertial Fusion (High-Gain MagLIF),” presented by Stephen Slutz at the Dense Z-Pinch (DZP) meeting in Biarritz, France, June 6-9, 2011.

“Radiography of magnetically-driven implosions of initially solid beryllium cylindrical shells for equation-of-state studies at the Z pulsed-power facility,” presented by Ryan McBride at the 17th Biennial International Conference of the APS Topical Group on Shock Compression of Condensed Matter in Chicago, Illinois, June 26-July 1, 2011.

“Penetrating radiography of imploding and stagnating beryllium liners on the Z accelerator,” to be presented by Ryan McBride at the American Physical Society Division of Plasma Physics (APS-DPP) meeting in Providence, RI, Oct. 29-Nov. 2, 2012.

5.2 Publications

Much of the work supported by this LDRD has already been published in peer-reviewed journals, and additional publications in the next few years on the work presented in this SAND report are expected. A list of publications directly supported by this LDRD project follows.

S.A. Slutz, M.C. Herrmann, R.A. Vesey, A.B. Sefkow, D.B. Sinars, D.C. Rovang, K.J. Peterson, and M.E. Cuneo, “Pulsed-power-driven cylindrical liner implosions of laser preheated fuel magnetized with an axial field,” *Physics of Plasmas* 17, 056303 (2010).

D.B. Sinars, S.A. Slutz, M.C. Herrmann, R.D. McBride, M.E. Cuneo, K.J. Peterson, R.A. Vesey, C. Nakhleh, B.E. Blue, K. Killebrew, D. Schroen, K. Tomlinson, A.D. Edens, M.R. Lopez, I.C. Smith, J. Shores, V. Bigman, G.R. Bennett, B.W. Atherton, M. Savage, W.A. Stygar, G.T. Leifeste, and J.L. Porter, “Measurements of magneto-Rayleigh-Taylor instability growth during the implosion of initially solid Al tubes driven by the 20-MA, 100-ns Z facility,” *Phys. Rev. Lett.* 105, 185001 (2010).

D.B. Sinars, S.A. Slutz, M.C. Herrmann, R.D. McBride, M.E. Cuneo, C.A. Jennings, J.P. Chittenden, A.L. Velikovich, K.J. Peterson, R.A. Vesey, C. Nakhleh, E.M. Waisman, B.E. Blue, K. Killebrew, D. Schroen, K. Tomlinson, A.D. Edens, M.R. Lopez, I.C. Smith, J. Shores, V. Bigman, G.R. Bennett, B.W. Atherton, M. Savage, W.A. Stygar, G.T. Leifeste, and J.L. Porter, “Measurements of magneto-Rayleigh-Taylor instability growth during the implosion of initially solid metal liners,” *Physics of Plasmas* 18, 056301 (2011).

R.W. Lemke, M.R. Martin, R.D. McBride, J.-P. Davis, M.D. Knudson, D.B. Sinars, I.C. Smith, M. Savage, W.A. Stygar, K. Killebrew, D.G. Flicker, and M.C. Herrmann, “Determination of pressure and density of shocklessly compressed beryllium from x-ray radiography of a magnetically-driven cylindrical liner implosion,” *AIP Conf. Proc.* 1426, 473 (2012).

M.R. Martin, R.W. Lemke, R.D. McBride, J.-P. Davis, and M.D. Knudson, “Analysis of cylindrical ramp compression experiment with radiography based surface fitting method,” *AIP Conf. Proc.* 1426, 357 (2012).

M.R. Martin, R.W. Lemke, R.D. McBride, J.-P. Davis, D.H. Dolan, M.D. Knudson, K.R. Cochrane, D.B. Sinars, I.C. Smith, M. Savage, W.A. Stygar, K. Killebrew, D.G. Flicker, and M.C. Herrmann, “Solid liner implosions on Z for producing multi-megabar, shockless compressions,” *Physics of Plasmas* 19, 056310 (2012).

S.A. Slutz and R.A. Vesey, “High-gain magnetized inertial fusion,” *Phys. Rev. Lett.* 108, 025003 (2012).

R.D. McBride, S.A. Slutz, C.A. Jennings, D.B. Sinars, M.E. Cuneo, M.C. Herrmann, R.W. Lemke, M.R. Martin, R.A. Vesey, K.J. Peterson, A.B. Sefkow, C. Nakhleh, B.E. Blue, K. Killebrew, D. Schroen, T.J. Rogers, A. Laspe, M.R. Lopez, I.C. Smith, B.W. Atherton, M. Savage, W.A. Stygar, and J.L. Porter, “Penetrating radiography of imploding and stagnating

beryllium liners on the Z accelerator,” accepted for publication in Physical Review Letters (2012).

R.D. McBride, S.A. Slutz, C.A. Jennings, D.B. Sinars, M.E. Cuneo, M.C. Herrmann, R.W. Lemke, M.R. Martin, R.A. Vesey, K.J. Peterson, A.B. Sefkow, C. Nakhleh, B.E. Blue, K. Killebrew, D. Schroen, T.J. Rogers, A. Laspe, M.R. Lopez, I.C. Smith, B.W. Atherton, M. Savage, W.A. Stygar, and J.L. Porter, “Beryllium liner implosion experiments on the Z accelerator in preparation for Magnetized Liner Inertial Fusion,” manuscript in preparation for submission to Physics of Plasmas as part of APS-DPP invited talk.

5.3 Awards received

This LDRD made significant contributions to several awards for both the team and for the principal investigator. They are as follows:

Defense Programs Award of Excellence presented to the “Magneto-Rayleigh-Taylor Experiments Team” for significant contributions to the Stockpile Stewardship Program, awarded June 2011.

Department of Energy Office of Science Early Career Research Program Award, given to outstanding university or national laboratory researchers within 10 years of their doctorates. The award was announced in May 2011 and provides \$2.5 million over 5 years to Daniel Sinars to enable the study of “Fundamental instability measurements in magnetically-driven Z-pinch liner implosions.”

2011 Presidential Early Career Award for Scientists and Engineers (PECASE) for Daniel Sinars (announced in July 2012), “For developing innovative techniques to study the properties of instabilities in magnetized-high-energy-density plasma, enabling quantifiable comparison between experiment and simulation needed for validating cutting-edge radiation-hydrodynamics codes, and for demonstrating substantial leadership qualities in high-energy-density-laboratory-plasma (HEDLP) physics.”

6. REFERENCES

1. M.K. Matzen, M.A. Sweeney, R.G. Adams, J.R. Asay, J.E. Bailey, G.R. Bennett, D.E. Bliss, D.D. Bloomquist, T.A. Brunner, R.B. Campbell, G.A. Chandler, C.A. Coverdale, M.E. Cuneo, J.-P. Davis, C. Deeney, M.P. Desjarlais, G.L. Donovan, C.J. Garasi, T.A. Hail, C.A. Hall, D.L. Hanson, M.J. Hurst, B. Jones, M.D. Knudson, R.J. Leeper, R.W. Lemke, M.G. Mazarakis, D.H. McDaniel, T.A. Mehlhorn, T.J. Nash, C.L. Olson, J.L. Porter, P.K. Rambo, S.E. Rosenthal, G.A. Rochau, L.E. Ruggles, C.L. Ruiz, T.W.L. Sanford, J.F. Seamen, D.B. Sinars, S.A. Slutz, I.C. Smith, K.W. Struve, W.A. Stygar, R.A. Vesey, E.A. Weinbrecht, D.F. Wenger, and E.P. Yu, "Pulsed-power-driven high energy density physics and inertial confinement fusion research," *Phys. Plasmas* 12, 055503 (2005).
2. R.A. Vesey, M.C. Herrmann, R.W. Lemke, M.P. Desjarlais, M.E. Cuneo, W.A. Stygar, G.R. Bennett, R.B. Campbell, P.J. Christenson, T.A. Mehlhorn, J.L. Porter, and S.A. Slutz, "Target design for high fusion yield with the double z-pinch-driven hohlraum," *Phys. Plasmas* 14, 056302 (2007).
3. S.A. Slutz, M.C. Herrmann, R.A. Vesey, A.B. Sefkow, D.B. Sinars, D.C. Rovang, K.J. Peterson, and M.E. Cuneo, "Pulsed-power-driven cylindrical liner implosions of laser preheated fuel magnetized with an axial field," *Phys. Plasmas* 17, 056303 (2010).
4. E.G. Harris, "Rayleigh-Taylor instabilities of a collapsing cylindrical shell in a magnetic field," *Phys. Fluids* 5, 1057 (1962).
5. R.E. Reinovsky *et al.*, *IEEE Trans. Plasma Sci.* 30, 1764 (2002).
6. D.B. Sinars, S.A. Slutz, M.C. Herrmann, R.D. McBride, M.E. Cuneo, K.J. Peterson, R.A. Vesey, C. Nakhleh, B.E. Blue, K. Killebrew, D. Schroen, K. Tomlinson, A.D. Edens, M.R. Lopez, I.C. Smith, J. Shores, V. Bigman, G.R. Bennett, B.W. Atherton, M. Savage, W.A. Stygar, G.T. Leifeste, and J.L. Porter, "Measurements of magneto-Rayleigh-Taylor instability growth during the implosion of initially solid Al tubes driven by the 20-MA, 100-ns Z facility," *Phys. Rev. Lett.* 105, 185001 (2010).
7. D.B. Sinars *et al.*, "Measurements of MRT instability growth during the implosion of initially solid metal liners," *Phys. Plasmas* 18, 056301 (2011).
8. R.W. Lemke *et al.*, "Determination of pressure and density of shocklessly compressed beryllium from x-ray radiography of a magnetically driven cylindrical liner implosion," *AIP Conf. Proc.* 1426, 473 (2012).
9. M.R. Martin *et al.*, "Analysis of cylindrical ramp compression experiment with radiography based surface fitting method," *AIP Conf. Proc.* 1426, 357 (2012).
10. M.R. Martin, R.W. Lemke, R.D. McBride, J.-P. Davis, D.H. Dolan, M.D. Knudson, K.R. Cochrane, D.B. Sinars, I.C. Smith, M. Savage, W.A. Stygar, K. Killebrew, D.G. Flicker, and M.C. Herrmann, "Solid liner implosions on Z for producing multi-megabar, shockless compressions," *Physics of Plasmas* 19, 056310 (2012).
11. R.D. McBride *et al.*, "Penetrating radiography of imploding and stagnating beryllium liners on the Z accelerator," *Phys. Rev. Lett.* (accepted Aug. 2012).
12. R.D. McBride *et al.*, "Beryllium liner implosion experiments on the Z accelerator in preparation for Magnetized Liner Inertial Fusion," invited talk manuscript in preparation for submission to *Physics of Plasmas* as part of October 2012 APS-DPP meeting.
13. S.A. Slutz & R.A. Vesey, "High-gain magnetized inertial fusion," *Phys. Rev. Lett.* 108, 025003 (2012).

14. D.B. Sinars, G.R. Bennett, D.F. Wenger, M.E. Cuneo, D.L. Hanson, J.L. Porter, R.G. Adams, P.K. Rambo, D.C. Rovang, and I.C. Smith, "Monochromatic x-ray imaging experiments on the Sandia National Laboratories Z facility (invited)," *Rev. Sci. Instrum.* 75, 3672 (2004).
15. D.B. Sinars, G.R. Bennett, M.C. Herrmann, I.C. Smith, C.S. Speas, L.E. Ruggles, and J.L. Porter, "Enhancement of x-ray yield from the Z-Beamlet laser for monochromatic backlighting by using a prepulse," *Rev. Sci. Instrum.* 77, 10E309 (2006).
16. G.R. Bennett, D.B. Sinars, D.F. Wenger *et al.*, "High-brightness, high-spatial-resolution, 6.151 keV x-ray imaging of inertial confinement fusion capsule implosion and complex hydrodynamics experiments on Sandia's Z accelerator (invited)," *Rev. Sci. Instrum.* 77, 10E322 (2006).
17. G.R. Bennett, I.C. Smith, J.E. Shores *et al.*, "2-20 ns interframe time 2-frame 6.151 keV x-ray imaging on the recently upgraded Z accelerator: A progress report," *Rev. Sci. Instrum.* 79, 10E914 (2008).
18. B. Jones, C. Deeney, J.L. McKenney, C.J. Garasi, T.A. Mehlhorn, A.C. Robinson, S.E. Wunsch, S.N. Bland, S.V. Lebedev, J.P. Chittenden, S.C. Bott, D.J. Ampleford, J.B.A. Palmer, J. Rapley, G.N. Hall, and B.V. Oliver, *Phys. Rev. Lett.* 95, 225001 (2005).
19. A.R. Piriz, J.J. Lopez Cela, O.D. Coryazar, N.A. Tahir, and D.H.H. Hoffman, *Phys. Rev. E* 72, 056313 (2005).
20. J.D. Colvin, M. Legrand, B.A. Remington, G. Schurtz, and S.V. Weber, *J. Appl. Phys.* 93(9), 5287 (2003).
21. A.C. Robinson and J.W. Swegle, *J. Appl. Phys.* 66(7), 2859 (1989).
22. A.C. Robinson, T.A. Brunner, S. Carrol *et al.*, "ALEGRA: An arbitrary Lagrangian-Eulerian multimaterial, multiphysics code," 46th AIAA Aerospace Sciences Meeting and Exhibit, Reno, NV, 2008; AIAA 2008-1235: p. 1-39.
23. N.B. Meezan, L. Divol, M.M. Marinak *et al.*, "Hydrodynamics simulations of 2-omega laser propagation in underdense gasbag plasmas," *Phys. Plasmas* 11, 5573 (2004).

DISTRIBUTION

1	MS0359	D. Chavez, LDRD Office	1911
1	MS0899	Technical Library	9536 (electronic copy)
1	MS1193	Daniel B. Sinars	01648



Sandia National Laboratories